


Article

Paleoproterozoic Crust–Mantle Interaction in the Khondalite Belt, North China Craton: Constraints from Geochronology, Elements, and Hf-O-Sr-Nd Isotopes of the Layered Complex in the Jining Terrane

Wei-Peng Zhu ^{1,2} , Wei Tian ^{1,*}, Bin Wang ¹, Ying-Hui Zhang ² and Chun-Jing Wei ¹

¹ MOE Key Laboratory of Orogenic Belts and Crustal Evolution, School of Earth and Space Sciences, Peking University, Beijing 100871, China

² Key Laboratory of Deep-Earth Dynamics of Ministry of Natural Resources, Institute of Geology, Chinese Academy of Geological Sciences, Beijing 100037, China

* Correspondence: davidtian@pku.edu.cn

Abstract: The Paleoproterozoic Khondalite Belt, located in the northwestern segment of North China Craton (NCC), is characterized by widespread high-temperature/ultrahigh-temperature (UHT) granulite/gneiss and large-scale magmatic activity. The tectonic evolution is still controversial. Here, we report new geochronological, elemental, and Hf-O-Sr-Nd isotopic data for a Paleoproterozoic layered complex in the Jining terrane to constrain the tectonic evolution of the Khondalite Belt. In situ zircon U-Pb dating indicates that the Sanchakou gabbros were emplaced between ~1.94 Ga and ~1.82 Ga, which might be the heat source of UHT metamorphism. The elemental and Hf-O-Sr-Nd isotopic analysis shows that the formation of Sanchakou gabbros is consistent with the assimilation and fractional crystallization (AFC) process. The magma originates from the 10%~20% partial melting of the spinel + garnet lherzolite mantle. The Sanchakou gabbros are magmatic crystallization products mixed with crustal wallrocks in the magma chamber. We have established a tectonic evolution model involving asthenosphere upwelling after the amalgamation of the Ordos and Yinshan Blocks at ~1.95 Ga.

Keywords: NCC; Paleoproterozoic Khondalite Belt; UHT granulite/gneiss; layered complex; AFC; tectonic evolution



Citation: Zhu, W.-P.; Tian, W.; Wang, B.; Zhang, Y.-H.; Wei, C.-J.

Paleoproterozoic Crust–Mantle Interaction in the Khondalite Belt, North China Craton: Constraints from Geochronology, Elements, and Hf-O-Sr-Nd Isotopes of the Layered Complex in the Jining Terrane.

Minerals **2023**, *13*, 462.

<https://doi.org/10.3390/min13040462>

min13040462

Academic Editors: Jin Liu, Jiahui Qian, Xiaoguang Liu and Dominique Gasquet

Received: 23 February 2023

Revised: 18 March 2023

Accepted: 21 March 2023

Published: 24 March 2023



Copyright: © 2023 by the authors. Licensee MDPI, Basel, Switzerland. This article is an open access article distributed under the terms and conditions of the Creative Commons Attribution (CC BY) license (<https://creativecommons.org/licenses/by/4.0/>).

1. Introduction

The concept of “layered complex” was first recorded in *Layered Igneous Rocks* [1]. Most of the layered complex is close to gabbros, mainly composed of basic or ultrabasic rocks. The most notable feature is the well-developed layered rhythmic structure. The layered complexes formed mainly in Archean and Proterozoic [2–6], with a lesser amount in Phanerozoic [7–9]. The tectonic environment is related to mantle plume or intracontinental rifting [10–13], controlled by regional fractures. Crustal contamination plays an important role in the formation of layered complexes, which can greatly change the composition of magma and result in the difference in products [14,15]. Therefore, the compositional changes in layered complexes in the open magmatic system are significant for revealing crust–mantle interaction [16–19].

The North China Craton (NCC) is a fundamental geological unit of the early Precambrian in China [20]. The Jining terrane, located in the eastern Khondalite Belt of the NCC, has been widely studied by researchers in past decades. A large number of ultrahigh-temperature (UHT) metamorphic rocks have been reported in this area [21–32]. In addition, there are small amounts of basic intrusive rocks dominated by gabbros, some of which occurred as multiple sets of layered complexes [33]. The episodic crystallization ages are 2.45~2.10 Ga, 1.97~1.92 Ga, and 1.85~1.84 Ga [34–37]. The magma may have originated

from a deep mantle of ~ 3.0 GPa, and ~ 1550 °C [35]. However, the genesis of these basic intrusive rocks and tectonic environment have not been determined yet.

In this paper, we focus on a Paleoproterozoic layered complex in the Jining area, northwestern margin of the NCC, which is accompanied by extensive granulites/gneisses. Through the chronological, elemental, and Hf-O-Sr-Nd isotopic analysis methods, we have found that the layered complex is a product of crust–mantle interaction, which reflects the large-scale thermal fluctuation under the influence of the upwelling asthenosphere.

2. Geological Setting

The NCC is one of the rare ancient continental blocks with ~ 3.8 Ga crustal rock in the world [38–40]. There are different views about the formation and evolution of the NCC [20,41,42]. The Khondalite Belt is in the western part of the NCC (Figure 1a), considered to be formed via a collision between the Ordos and Yinshan Blocks at ~ 1.95 Ga [20,43]. From west to east, there are Qianlishan-Helanshan terrane, Daqingshan-Helanshan terrane, and Jining terrane. The Jining terrane is located in the eastern segment of the Khondalite Belt (Figure 1b), where UHT granulites/gneisses, S-type granites, and a small amount of basic intrusive rocks are mainly exposed (Figure 1c).

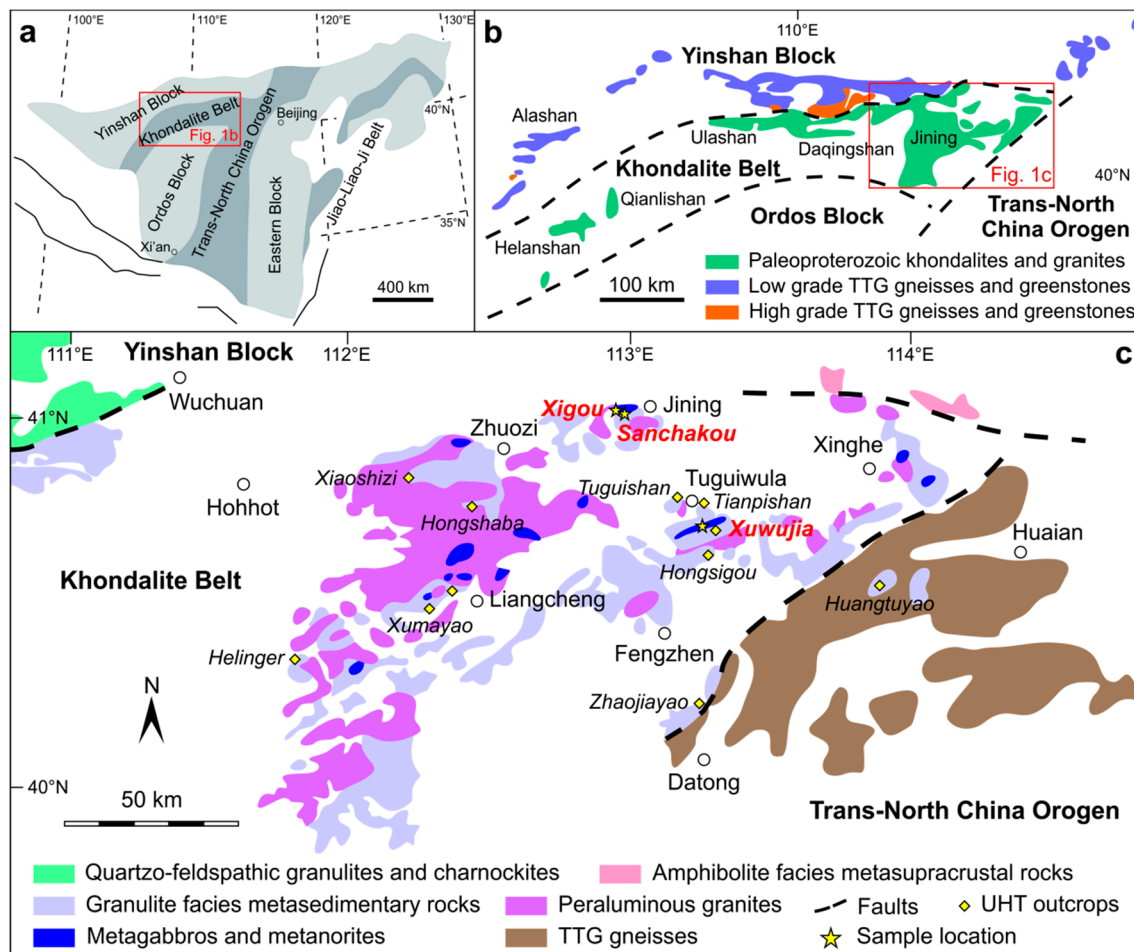


Figure 1. The regional geological map of the Jining terrane in the Khondalite Belt of the NCC. (a) The structural sketch of the NCC (modified from [20]); (b) The distribution map of structural units contained in the Khondalite Belt and adjacent structural units of the Khondalite Belt (modified from [20]); (c) The lithology distribution map of the Jining terrane (modified from [34]).

The UHT granulites/gneisses are scattered in Tuguishan, Dajing, Tianpishan, Xuwujia, Xumayao, Helinger, Hongsigou, Zhaojiayao, Liangcheng, and Hongshaba [23–26,28–31,44–50],

continuously forming a UHT metamorphic zone of about 250×150 square kilometers. Most of these UHT granulites/gneisses are sillimanite-garnet gneisses, and only a few contain spinel/sapphirine + quartz assemblages. They have average metamorphic ages of 1.92–1.91 Ga [30,31,44,50] and ~1.88 Ga [28]. The peak temperature of UHT metamorphism is mainly concentrated at 950–1050 °C [23–26,28–31,44–50].

The vast majority of the S-type granites are garnet granites, which intruded into the khondalite and covered more than 40% of the Jining terrane. The crystallization age is about 1.94–1.90 Ga [51,52]. One view [51] believed that garnet granite is a mixture of the mantle-derived basic magma and the melt produced by the anatexis of metasedimentary rocks, formed in the process of UHT metamorphism (1.93–1.92 Ga). The other view [52] believed that the garnet granite was formed before UHT metamorphism (1.94–1.93 Ga) and underwent UHT metamorphism (~1.92 Ga) with metasedimentary rocks.

A few basic intrusive rocks are mainly gabbros with an average crystallization age of ~1.93 Ga, believed to originate from the mantle plume or mantle upwelling under the background of the mid-ocean ridge [35].

3. Samples and Methods

3.1. Sample Description

The studied sample is from a drilling core of the layered complex, taken from Sanchakou town, Jining District, Ulanqab City, Inner Mongolia Autonomous Region (Figure 1c). We selected a section in which the overall lithology is gabbro, with obvious changes in feldspar content in the vertical direction (Figure 2a). Therefore, the layered complex was named the Sanchakou gabbros. We chose typical positions of the drilling core, cut into rock thin slices, ground the rock into powder, and numbered SCK-1 to SCK-6, respectively.

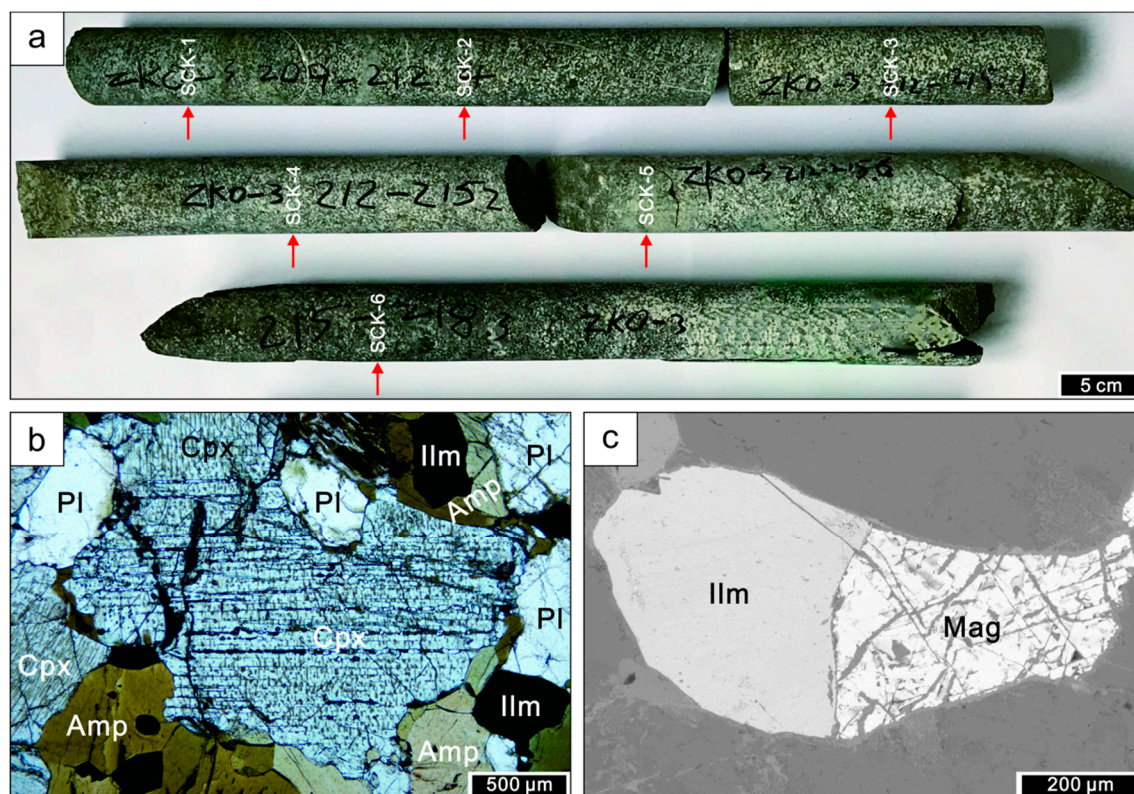


Figure 2. Petrological characteristics of the Sanchakou gabbros from the Jining terrane. (a) The Sanchakou gabbro drilling core (The arrows indicate the slicing and sampling positions); (b) The main rock-forming minerals, including the diopside, pargasite, and plagioclase; (c) The equilibrium assemblage of magnetite and ilmenite. Mineral abbreviations: Amp, amphibole; Cpx, clinopyroxene; Ilm, ilmenite; Mag, magnetite; Pl, plagioclase.

The rock has a full-crystalline unequal granular texture. The main minerals include clinopyroxene, amphibole, and plagioclase. The altered minerals mainly include zoisite and epidote. The representative accessory minerals include ilmenite, magnetite, apatite, and zircon. The clinopyroxene is mostly irregular prismatic, widely developing a group of parallel cleavage (Figure 2b). The amphibole has obvious pleochroism, and its interference color is lower than that of the clinopyroxene. The primary amphibole is generally subhedral plate-prismatic. The secondary amphibole is in a xenomorphic long-prismatic shape, growing along the edge of other minerals. The plagioclase has undergone intense zoisitization and idolization alteration. The opaque minerals mainly include ilmenite and magnetite, some of which form the equilibrium assemblages (Figure 2c). The apatite is transparent and round. The zircon is subhedral long-prismatic, developing a higher white interference color.

3.2. Analytical Methods

3.2.1. Mineral Major Elements Analysis

Mineral major elemental analysis was conducted by EPMA at the MOE Key Laboratory of Orogenic Belts and Crustal Evolution, School of Earth and Space Sciences, Peking University, Beijing, China. We used JEOL JXA-8230 for in situ analysis, equipped with four-channel spectrometers (CH₁-CH₄). PETJ crystal (CH₁) was used to determine K, Ca, and Ti. Two TAP crystals (CH₂, CH₄) were used to determine Na, Si, Mg, and Al. LIFH crystal (CH₃) was used to determine Cr, Mn, Fe, and Ni. The acceleration voltage, the beam current, and the beam spot were set to 15 kV, 10 nA, and 2 μm. The counting times for the background and peak values of Ca, Mg, Al, and Fe are 5 s and 20 s, and those of other elements are 5 s and 10 s. The standard samples are 53 kinds of minerals from American Structure Probe Inc. SuppliesTM Company. We used the stoichiometric method to calculate and the PRZ method to correct. Detailed information for the configuration of crystal spectrometers and the mineral standard samples of related elements was the same as described by [53].

3.2.2. In Situ Zircon U-Pb Isotopic Analysis

In situ zircon U-Pb isotopic analysis was conducted by LA-ICP-MS at the Wuhan SampleSolution Analytical Technology Company Limited, Hubei, China. Detailed operating conditions for the laser ablation system and the ICP-MS instrument were the same as described by [54]. Laser sampling was performed using a GeolasPro laser ablation system that consists of a COMPexPro 102 ArF excimer laser (wavelength of 193 nm and maximum energy of 200 mJ) and a MicroLas optical system. We used an Agilent 7900 ICP-MS instrument to acquire ion-signal intensities. Helium was applied as a carrier gas. Argon was used as the make-up gas and mixed with the carrier gas via a T-connector before entering the ICP. A “wire” signal smoothing device is included in this laser ablation system [55]. The spot size and frequency of the laser were set to 24 μm and 5 Hz. International zircon standard 91500 and glass NIST610 were used as external standards for U-Pb dating and trace element calibration, respectively. TEMORA-2 was treated as a blind sample to monitor the working state of the instrument. Each analysis incorporated a background acquisition of approximately 20~30 s followed by 50 s of data acquisition from the sample. We used ICPMSDataCal to perform offline selection and integration of background and analyze signals, time-drift correction, and quantitative calibration [56,57]. Concordia diagrams, probability density diagrams, and weighted mean calculations were made using Isoplot 4.15 [58].

3.2.3. Whole-Rock Major and Trace Elements Analysis

Whole-rock chemical pretreatment and major and trace element analysis were conducted at Nanjing FocuMS Technology Company Limited, Jiangsu, China. For major elements, we adopt the acid dissolution method to dissolve the sample powder to analyze the major elements except for Si and the alkali fusion method to liquate the sample powder

to analyze Si. The analytical instrument was Agilent 5110 ICP-OES. The analysis accuracy of SiO_2 is better than 1%; that of Al_2O_3 , TFeO , MgO , K_2O , Na_2O , and CaO is better than 3%; and that of TiO_2 , MnO , and P_2O_5 is better than 5%. For trace elements, we adopt the acid dissolution method to dissolve the sample powder. The analytical instrument was Agilent 7700x ICP-MS. Among them, the analysis accuracy of trace elements with content more than 50×10^{-6} is better than 5%; that of trace elements with content between 5×10^{-6} and 50×10^{-6} is better than 10%; and that of trace elements with content between 0.5×10^{-6} and 5×10^{-6} is better than 20%. Geochemical reference materials of BHVO-2 and AGV-2 were treated as blind samples for quality assurance of measurement, the measured values of which were compared with *Geological and Environmental Reference Materials* (GeoReM) [59]. The detailed operating process was the same as described by [60].

3.2.4. In Situ Zircon Hf-O Isotopic Analysis

In situ zircon Hf isotope ratio analysis was conducted using a Neptune Plus MC-ICP-MS in combination with a Geolas HD excimer ArF laser ablation system that was hosted at the Wuhan SampleSolution Analytical Technology Company Limited, Hubei, China. A “wire” signal smoothing device is included in this laser ablation system, by which smooth signals are produced even at very low laser repetition rates down to 1 Hz [55]. Helium was used as the carrier gas within the ablation cell and was merged with argon after the ablation cell. Small amounts of nitrogen were added to the argon makeup gas flow for sensitivity improvement [61]. The single spot size and energy density of the laser were set to $32 \mu\text{m}$ and $\sim 7.0 \text{ J cm}^{-2}$. Each measurement included 20 s of background signal acquisition and 50 s of ablation signal acquisition. Detailed operating conditions for the laser ablation system, the MC-ICP-MS instrument, and the analytical method were the same as described by [61]. The interference of ^{176}Lu and ^{176}Yb on ^{176}Hf was corrected according to [62]. Off-line selection and integration of analytical signal and mass bias calibrations were performed using ICPMSDataCal [57]. To ensure the data reliability, three international zircon standards of Plešovice, 91500, and GJ-1 were analyzed simultaneously with the actual samples, the Hf isotopic compositions of which have been reported by [63]. The external accuracies (2σ) of Plešovice, 91500, and GJ-1 were better than 0.000020. The test values were consistent with the recommended value within the error range.

In situ zircon O isotopic analysis was conducted using a SHRIMP IIe-MC that was hosted at the Beijing SHRIMP Center, Institute of Geology, Chinese Academy of Geological Sciences, Beijing, China. Detailed operating conditions were the same as described by [64,65]. Two groups of scans were set for each data analysis. Each group was scanned 6 times, and the integral time of each scan was 10 s. Between the two groups of scans, the instrument can automatically readjust the parameters of the primary ion current and the secondary ion current to achieve the best result. During the analysis process, the ratio of sample zircon data points to standard zircon data points was 1:2~1:4. The internal accuracy of single analysis data was generally better than $\pm 0.3\%$ (2σ). We used TEMORA-2 ($\delta^{18}\text{O} = 8.20\%$) [66] and 91500 ($\delta^{18}\text{O} = 9.86\%$) [67] to monitor the working state of the instrument and correct for the mass fractionation. *Vienna standard mean ocean water* (V-SMOW) was adopted to standardize the O isotopic analysis results.

In particular, the zircon number and position of in situ Hf-O isotopic analysis were consistent with those of in situ U-Pb isotopic analysis.

3.2.5. Whole-Rock Sr-Nd Isotopic Analysis

Whole-rock chemical pretreatment and Sr-Nd isotopic analysis were conducted at Nanjing FocuMS Technology Company Limited, Jiangsu, China. We adopt the acid dissolution method to dissolve the sample powder, followed by extraction and chromatographic separation according to the method of [68]. The detailed operating process was the same as described by [69]. The analytical instrument was Nu Plasma II MC-ICP-MS. Raw data of isotope ratios were internally corrected for the mass fractionation by normalizing $^{86}\text{Sr}/^{88}\text{Sr} = 0.1194$ for Sr, $^{146}\text{Nd}/^{144}\text{Nd} = 0.7219$ for Nd with exponential law. International

isotopic standards (NIST SRM 987 for Sr, JNdi-1 for Nd) were periodically analyzed to correct instrumental drift. Geochemical reference materials of BCR-2 and BHVO-2 were treated as blind samples for quality assurance of measurement. These isotopic results agreed with previous publications regarding analytical uncertainty [70].

4. Results

4.1. Mineral Chemistry

The EPMA analytical results of clinopyroxene, amphibole, plagioclase, magnetite, and ilmenite in the Sanchakou gabbros are listed in Table 1.

Table 1. The major elemental data (wt.%) of representative minerals in the Sanchakou gabbros.

Mineral	SiO ₂	TiO ₂	Al ₂ O ₃	Cr ₂ O ₃	TFeO	MnO	NiO	MgO	CaO	Na ₂ O	K ₂ O	Total
Cpx	52.42	0.25	1.99	0.01	8.09	0.36	0.01	14.05	23.87	0.39	0.01	101.45
Amp	43.89	2.01	10.65	0.03	13.03	0.21	0.02	12.98	12.38	1.46	1.21	97.87
Pl	55.91	0.01	28.08	0.01	0.15	0.01	0.03	0	11.17	5.11	0.25	100.73
Mag	0.31	0.10	0.17	0.04	93.65	0.02	0.01	0.14	0.11	0.06	0.01	94.62
Ilm	0.03	50.58	0.03	0.02	46.29	2.63	0.01	0.05	0.01	0.03	0.00	99.68

Notes: Amp, amphibole; Cpx, clinopyroxene; Ilm, ilmenite; Mag, magnetite; Pl, plagioclase.

4.1.1. Clinopyroxene

According to the classification of [71], the clinopyroxene of Sanchakou gabbros corresponds to the Ca-Mg-Fe pyroxenes (Figure 3a). Its composition is Wo_{46.71–47.48}En_{36.26–39.35}Fs_{12.17–14.74}, belonging to the diopside (Figure 3b). The Mg[#] of the clinopyroxene ranges from 72.11 to 77.20, with an average value of 75.58. The Cr[#] is mostly 0. The clinopyroxene has relatively low contents of TiO₂ (0.14–0.56 wt.%), Al₂O₃ (1.42–3.61 wt.%), TFeO (7.57–8.97 wt.%), and Na₂O (0.30–0.55 wt.%).

4.1.2. Amphibole

The amphibole of Sanchakou gabbros has relatively high contents of Al₂O₃ (10.14–10.97 wt.%), TFeO (12.12–14.12 wt.%), MgO (12.30–13.84 wt.%), and CaO (11.76–12.86 wt.%) and relatively low contents of SiO₂ (42.15–45.53 wt.%), Na₂O (1.21–1.61 wt.%), and K₂O (0.96–1.32 wt.%). In general, its composition has little change. According to the classification of [72], the amphibole belongs to the pargasite and edenite (Figure 3c).

4.1.3. Plagioclase

The plagioclase of Sanchakou gabbros has relatively high contents of Al₂O₃ (27.46–29.03 wt.%) and CaO (10.49–11.94 wt.%) and a relatively low content of K₂O (0.14–0.35 wt.%). Its composition is An_{50.20–57.16}Ab_{41.42–48.12}Or_{0.80–1.99}. According to the classification of [73], the plagioclase belongs to the labradorite (Figure 3d).

4.2. In Situ Zircon Isotopic Characteristics

4.2.1. Zircon U-Pb Dating

The in situ zircon U-Pb isotopic data of the Sanchakou gabbros are listed in Table 2. The zircons selected from the Sanchakou gabbros are irregularly rounded crystals, ranging from 70 μm to 180 μm in diameter. Almost all zircons have bright growth edges in CL images, which vary in width (Figure 4a). The core of zircons is generally dark. A few of the cores have obvious growth stripes inside. Small amounts of zircons have 2225–2375 Ma inherited cores. All characteristics reflect the crystallization history of zircons and the superposition of multi-stage magmatism. The zircon Th/U ratios range from 0.11 to 7.53, with an average value of 1.44. Based on these features, the zircon belongs to the magmatic zircon.

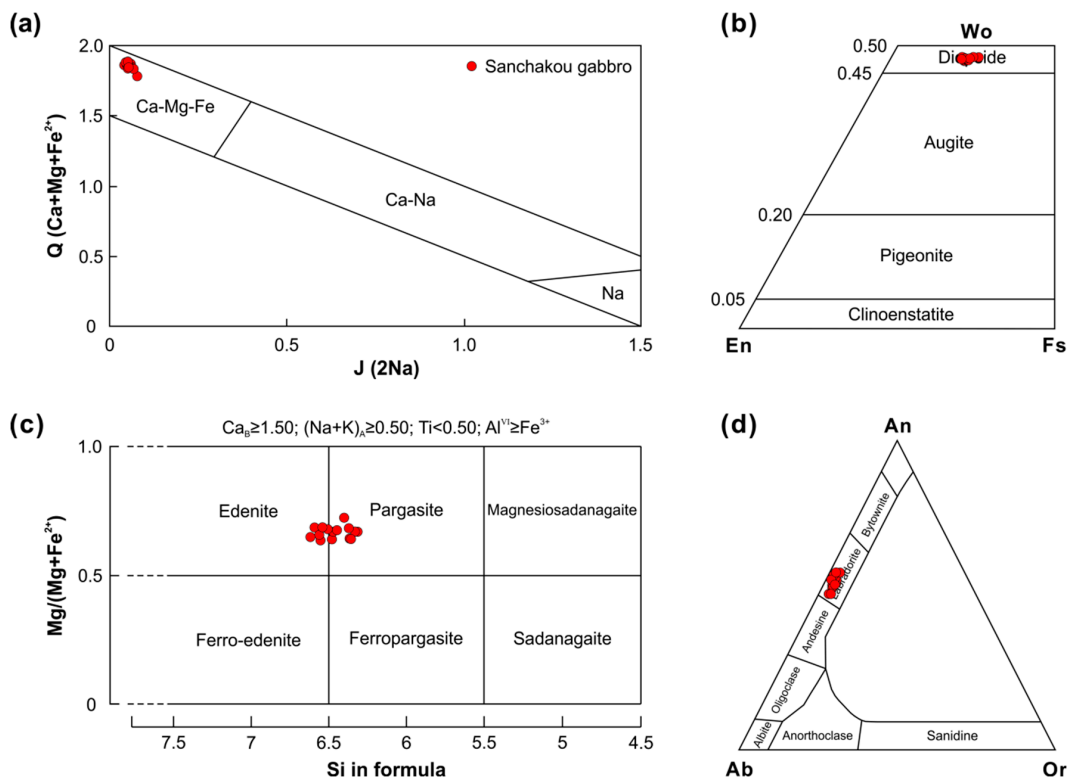


Figure 3. Mineral compositions of the Sanchakou gabbros from the Jining terrane. (a) The Q-J diagram of pyroxene according to the nomenclature of [71]; (b) The classification diagram of pyroxene according to the nomenclature of [71]; (c) The classification diagram of amphibole according to the nomenclature of [72]; (d) The classification diagram of feldspar according to the nomenclature of [73]. Mineral abbreviations: Ab, albite; An, anorthite; En, enstatite; Fs, ferrosilite; Or, potassium feldspar; Wo, wollastonite.

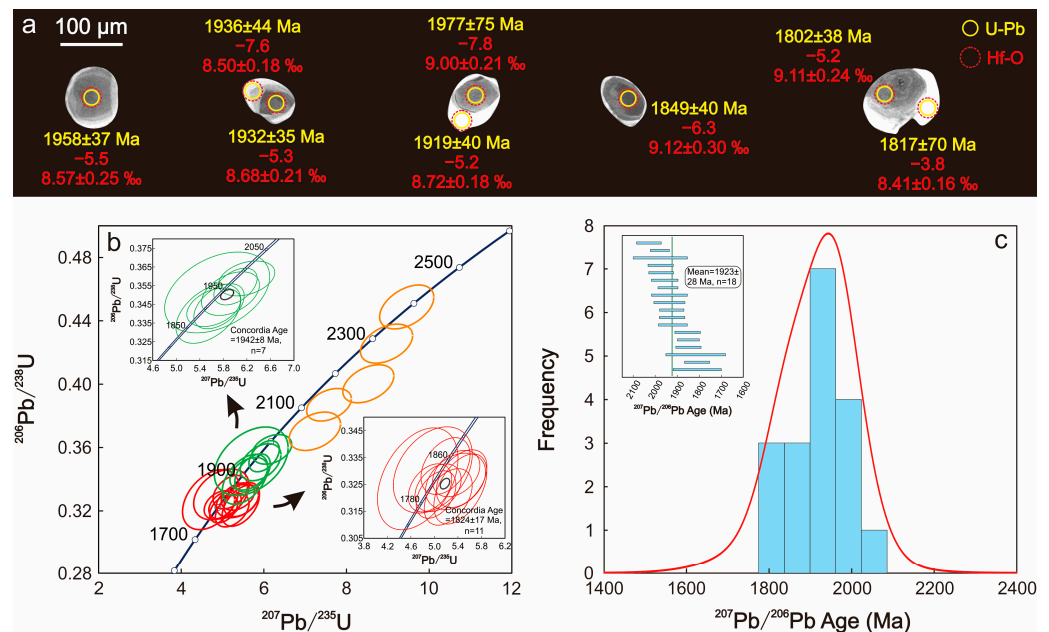


Figure 4. Zircon U-Pb isotopic analytical results of the Sanchakou gabbros from the Jining terrane. (a) Typical zircon CL images, marked with spot positions of in situ zircon U-Pb and Hf-O isotopic analysis; (b) The zircon U-Pb concordia diagram; (c) The $^{207}\text{Pb}/^{206}\text{Pb}$ age probability density histogram together with the $^{207}\text{Pb}/^{206}\text{Pb}$ weighted average age distribution.

Table 2. The in situ zircon U-Pb isotopic data of the Sanchakou gabbros.

Sample	Th ($\times 10^{-6}$)	U ($\times 10^{-6}$)	Th/U	$^{207}\text{Pb}/^{206}\text{Pb}$	$\pm 1\sigma$	$^{207}\text{Pb}/^{235}\text{U}$	$\pm 1\sigma$	$^{206}\text{Pb}/^{238}\text{U}$	$\pm 1\sigma$	$^{207}\text{Pb}/^{206}\text{Pb}$ Age (Ma)	$\pm 1\sigma$	Corrected $^{207}\text{Pb}/^{206}\text{Pb}$ Age (Ma)	$\pm 1\sigma$
SCK-1	98.74	146.87	0.67	0.1201	0.0025	5.4627	0.1757	0.3271	0.0044	1958	60	1958	37
SCK-2.1	31.93	280.56	0.11	0.1184	0.0024	5.5976	0.1810	0.3429	0.0050	1943	45	1932	35
SCK-2.2	99.94	42.62	2.34	0.1187	0.0030	5.5456	0.2253	0.3400	0.0065	1936	81	1936	44
SCK-3.1	286.49	529.80	0.54	0.1196	0.0026	5.8190	0.1880	0.3529	0.0043	1979	43	1950	38
SCK-3.2	84.66	110.80	0.76	0.1212	0.0025	5.4406	0.1839	0.3233	0.0053	1976	57	1974	36
SCK-4.1	79.50	149.93	0.53	0.1399	0.0033	7.2351	0.2538	0.3703	0.0050	2226	56	2225	41
SCK-4.2	112.83	82.50	1.37	0.1187	0.0033	5.3588	0.2084	0.3262	0.0043	1936	71	1936	49
SCK-5.1	175.25	349.17	0.50	0.1526	0.0029	8.5282	0.2523	0.4003	0.0049	2376	46	2375	32
SCK-5.2	70.99	95.85	0.74	0.1136	0.0037	4.9834	0.2247	0.3182	0.0047	1924	58	1924	57
SCK-6	97.22	265.73	0.37	0.1505	0.0032	8.8052	0.2818	0.4242	0.0053	2355	48	2352	36
SCK-8.1	91.48	13.31	6.87	0.1214	0.0052	5.6946	0.3648	0.3514	0.0088	1977	123	1977	75
SCK-8.2	65.32	164.50	0.40	0.1175	0.0027	5.6357	0.1866	0.3434	0.0042	1920	66	1919	40
SCK-9.1	126.56	162.62	0.78	0.1405	0.0028	7.5763	0.2212	0.3870	0.0042	2235	50	2234	34
SCK-9.2	68.40	113.10	0.60	0.1212	0.0027	5.9214	0.2012	0.3507	0.0048	1974	56	1974	40
SCK-10.1	127.14	248.59	0.51	0.1516	0.0027	9.4564	0.2680	0.4488	0.0057	2365	46	2364	30
SCK-10.2	155.94	183.12	0.85	0.1180	0.0025	5.3711	0.1641	0.3291	0.0035	1926	55	1926	38
SCK-11	78.17	140.98	0.55	0.1131	0.0025	5.0615	0.1605	0.3238	0.0036	1850	57	1849	40
SCK-12.1	110.85	271.20	0.41	0.1250	0.0028	6.1952	0.1955	0.3589	0.0038	2029	56	2029	39
SCK-12.2	172.81	136.29	1.27	0.1133	0.0025	5.1886	0.1703	0.3318	0.0043	1854	58	1853	39
SCK-12.3	94.04	21.42	4.39	0.1107	0.0042	4.9726	0.2740	0.3304	0.0066	1810	109	1810	68
SCK-13.1	95.48	133.61	0.71	0.1101	0.0023	4.9251	0.1510	0.3237	0.0037	1811	57	1802	38
SCK-13.2	104.55	13.89	7.53	0.1111	0.0044	4.7167	0.2796	0.3271	0.0077	1817	136	1817	70
SCK-14	62.50	193.00	0.32	0.1130	0.0020	5.0281	0.1381	0.3212	0.0036	1850	50	1848	32

Except for the data of inheritance cores, the rest zircon grains show a “beaded” distribution along the concordia line (Figure 4b). Based on the principle of statistics, the data can be divided into two groups: the concordia age of the first group is 1942 ± 8 Ma ($n = 7$) and the concordia age of the second group is 1824 ± 17 Ma ($n = 11$). The distribution of corrected $^{207}\text{Pb}/^{206}\text{Pb}$ apparent ages ranges from 1802 ± 38 Ma to 2029 ± 39 Ma. The $^{207}\text{Pb}/^{206}\text{Pb}$ weighted average age is concentrated at 1923 ± 28 Ma ($n = 18$). The $^{207}\text{Pb}/^{206}\text{Pb}$ age probability density histogram shows that the data distribution is continuous (Figure 4c), and the peak value is 1941 ± 22 Ma ($n = 18$).

4.2.2. Zircon Hf-O Isotopes

The in situ zircon Hf-O isotopic data of the Sanchakou gabbros are listed in Table 3.

Table 3. The in situ zircon Hf-O isotopic data of the Sanchakou gabbros.

Sample	$^{207}\text{Pb}/^{206}\text{Pb}$ Age (Ma)	$^{176}\text{Lu}/^{177}\text{Hf}$	$\pm 2\sigma$	$^{176}\text{Hf}/^{177}\text{Hf}$	$\pm 2\sigma$	$\epsilon_{\text{Hf}}(\text{t})$	$\epsilon_{\text{Hf}}(\text{0})$	$\pm 2\sigma$	TDM (Ma)	$\delta^{18}\text{O}$ (‰)	$\pm 2\sigma$
SCK-1	1958	0.000770	0.000020	0.281411	0.000012	−5.5	−48.1	0.4	2558	8.57	0.25
SCK-2.1	1943	0.000738	0.000006	0.281396	0.000012	−5.3	−47.1	0.4	2526	8.68	0.21
SCK-2.2	1936	0.000383	0.000004	0.281424	0.000012	−7.6	−47.8	0.4	2546	8.50	0.18
SCK-3.1	1979	0.000995	0.000026	0.281385	0.000013	−3.9	−48.7	0.4	2553	8.29	0.17
SCK-3.2	1976	0.000563	0.000013	0.281403	0.000012	−7.1	−48.2	0.4	2520	9.06	0.28
SCK-4.2	1936	0.000609	0.000047	0.281388	0.000013	−8.4	−48.5	0.5	2531	8.87	0.20
SCK-5.2	1924	0.000355	0.000016	0.281407	0.000012	−7.4	−47.7	0.4	2493	9.04	0.26
SCK-8.1	1977	0.000839	0.000001	0.281446	0.000012	−7.8	−48.2	0.5	2512	9.00	0.21
SCK-8.2	1920	0.000042	0.000001	0.281418	0.000012	−5.2	−46.1	0.5	2444	8.72	0.18
SCK-9.2	1974	0.000744	0.000007	0.281383	0.000013	−6.3	−48.6	0.4	2576	8.38	0.27
SCK-10.2	1926	0.000858	0.000005	0.281439	0.000012	−5.0	−47.7	0.4	2516	8.84	0.24
SCK-11	1850	0.000761	0.000004	0.281420	0.000012	−6.3	−49.1	0.5	2609	9.12	0.30
SCK-12.1	2029	0.000329	0.000023	0.281394	0.000012	−5.1	−48.4	0.4	2555	8.08	0.19
SCK-12.2	1854	0.000139	0.000002	0.281409	0.000012	−6.6	−48.9	0.5	2578	8.78	0.25
SCK-12.3	1810	0.000152	0.000002	0.281402	0.000015	−5.9	−48.3	0.4	2536	9.22	0.16
SCK-13.1	1811	0.000031	0.000001	0.281424	0.000011	−5.2	−46.9	0.4	2515	9.11	0.24
SCK-13.2	1817	0.000011	0.000000	0.281408	0.000013	−3.8	−47.9	0.4	2501	8.41	0.16
SCK-14	1850	0.000187	0.000012	0.281468	0.000013	−6.1	−49.1	0.5	2595	9.26	0.21

The zircon has a high Hf content and a very low Lu content, resulting in a very low $^{176}\text{Lu}/^{177}\text{Hf}$ ratio and a very low content of ^{176}Hf formed by Lu decay. So, there is no obvious radioactive accumulation after the formation of zircon. The $^{176}\text{Hf}/^{177}\text{Hf}$ measured in the samples can represent the Hf isotopic composition of the system when the zircons formed. The initial $^{176}\text{Hf}/^{177}\text{Hf}$ value of zircon in the samples is low (0.281383~0.281468), and the weighted average value is 0.281413 ± 0.000011 . The $\epsilon_{\text{Hf}}(\text{t})$ values are all negative, ranging from $−8.4$ to $−3.8$ (Figure 5a). The Lu-Hf T_{DM} age ranges from 2444 Ma to 2609 Ma, which belongs to the Paleoproterozoic and Archean, indicating that the magma may have originated from the enriched mantle or suffered from crustal contamination [74].

The zircon $\delta^{18}\text{O}$ value of the samples ranges from 8.08 to 9.26, with a weighted average value of $8.75 \pm 0.16\text{‰}$ (Figure 5b), which is much higher than that of the mantle zircon ($5.3 \pm 0.6\text{‰}$) [75]. Its genesis may be that the parent magmatic source of the Sanchakou gabbros was added with the high- $\delta^{18}\text{O}$ crustal materials, or the parent magma suffered from contamination by high- $\delta^{18}\text{O}$ crustal wallrocks during emplacement.

4.3. Whole-Rock Geochemical Characteristics

4.3.1. Major Elements

The whole-rock major elemental data of the Sanchakou gabbros are listed in Table 4. The loss on ignition (LOI) of the Sanchakou gabbros is negative, indicating that the samples have suffered from a low degree of alteration. It is consistent with the relatively fresh characteristics observed in the field. The content of SiO_2 is 43.45~45.01 wt.%, indicating that the samples belong to the basic rocks. The samples contain 12.73~13.64 wt.% Al_2O_3 , 0.14~0.23 wt.% K_2O , and 2.05~2.25 wt.% Na_2O . The content of $\text{Na}_2\text{O} + \text{K}_2\text{O}$ is 2.21~2.47 wt.%, and the ratio of $\text{K}_2\text{O}/\text{Na}_2\text{O}$ is 0.06~0.10, indicating that the samples belong

to calc-alkaline gabbros and have not suffered obvious potassium metasomatism. The samples fall into the peridot-gabbro field in the (Na₂O + K₂O)-SiO₂ diagram (Figure 6a) and the medium-K calc-alkaline series field in the K₂O-SiO₂ diagram (Figure 6b). The samples contain 7.44~7.77 wt.% MgO and 17.17~20.27 wt.% TFeO. The Mg[#] of the samples ranges from 40.08 to 44.64, with an average value of 41.78. The Mg[#] is relatively low, indicating that the Sanchakou gabbros were not formed in primary magma. The content of TiO₂ is 2.06~2.65 wt.%, which is higher than that of the high-K alkaline and shoshonitic rocks, indicating that the Sanchakou gabbros should originate from the mantle.

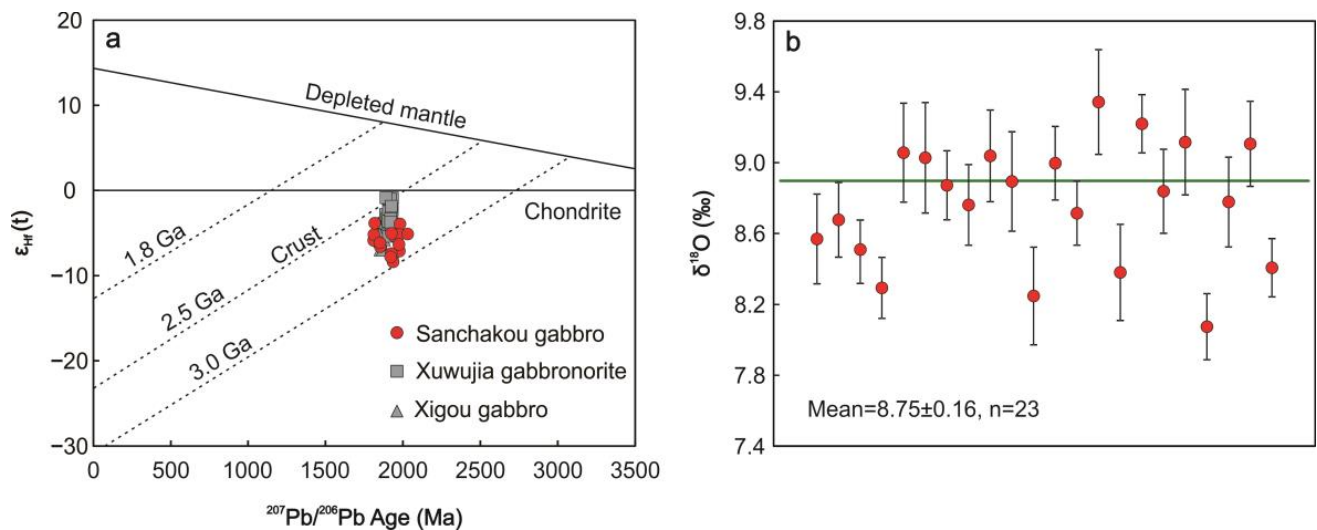


Figure 5. Zircon Hf-O isotopic compositions for the Sanchakou gabbros. (a) The $\epsilon_{\text{Hf}}(t)$ versus $^{207}\text{Pb}/^{206}\text{Pb}$ age diagram; (b) The $\delta^{18}\text{O}$ weighted average value distribution diagram. The Hf isotopic data of Xuwujia gabbro and Xigou gabbros are from [35,76].

Table 4. The whole-rock major elemental data (wt.%) of the Sanchakou gabbros.

Sample	SCK-1	SCK-2	SCK-3	SCK-4	SCK-5	SCK-6
SiO ₂	45.01	44.87	43.89	43.45	43.75	43.50
TiO ₂	2.06	2.29	2.46	2.65	2.52	2.59
Al ₂ O ₃	13.64	13.50	13.11	12.73	13.04	13.15
TFeO	17.17	17.87	19.18	20.27	19.20	19.96
MnO	0.26	0.27	0.27	0.28	0.26	0.28
MgO	7.77	7.61	7.68	7.61	7.44	7.56
CaO	11.41	11.09	11.17	10.79	11.38	10.46
Na ₂ O	2.25	2.24	2.12	2.05	2.13	2.17
K ₂ O	0.23	0.17	0.21	0.16	0.19	0.14
P ₂ O ₅	0.21	0.23	0.25	0.27	0.26	0.27
LOI	-0.14	-0.24	-0.24	-0.33	-0.14	-0.01
Total	99.86	99.90	100.08	99.94	100.02	100.08
Na ₂ O + K ₂ O	2.47	2.41	2.33	2.21	2.32	2.31
K ₂ O/Na ₂ O	0.10	0.08	0.10	0.08	0.09	0.06
Mg [#]	44.64	43.16	41.66	40.08	40.84	40.32
CaO/Al ₂ O ₃	0.84	0.82	0.85	0.85	0.87	0.80

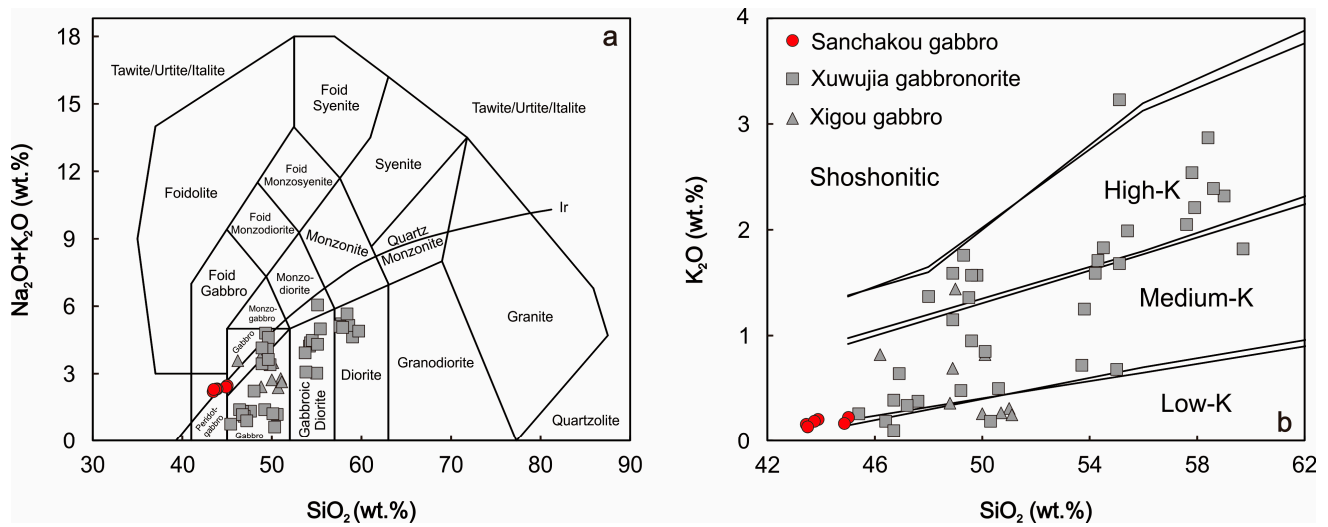


Figure 6. Binary classification diagrams for the Sanchakou gabbros. (a) The $(\text{Na}_2\text{O} + \text{K}_2\text{O})$ versus SiO_2 diagram [77]; (b) The K_2O versus SiO_2 diagram [78]. The major elemental data of Xuwujia gabbronorites and Xigou gabbros are from [35].

4.3.2. Trace Elements

The whole-rock trace elemental data of the Sanchakou gabbros are listed in Table 5. In the primitive mantle-normalized trace elements patterns of the Sanchakou gabbros, it is generally shown that Ba, K, Nb, Ta, Sr, and Ti are enriched, while Th and U are depleted (Figure 7a). In the chondrite-normalized rare earth elements (REE) patterns of the Sanchakou gabbros, the curve has a slightly right-leaning trend (Figure 7b). The total amount of REE (ΣREE) is not high, ranging from 58.6×10^{-6} to 77.40×10^{-6} , with an average value of 68.51×10^{-6} . The LREE/HREE ratio is 2.30~2.84, and the $(\text{La}/\text{Yb})_N$ ratio is 1.37~1.88, indicating that the LREE and the HREE of the samples are not differentiated. The δEu value is 0.95~1.08, indicating that the samples have no obvious Eu anomaly.

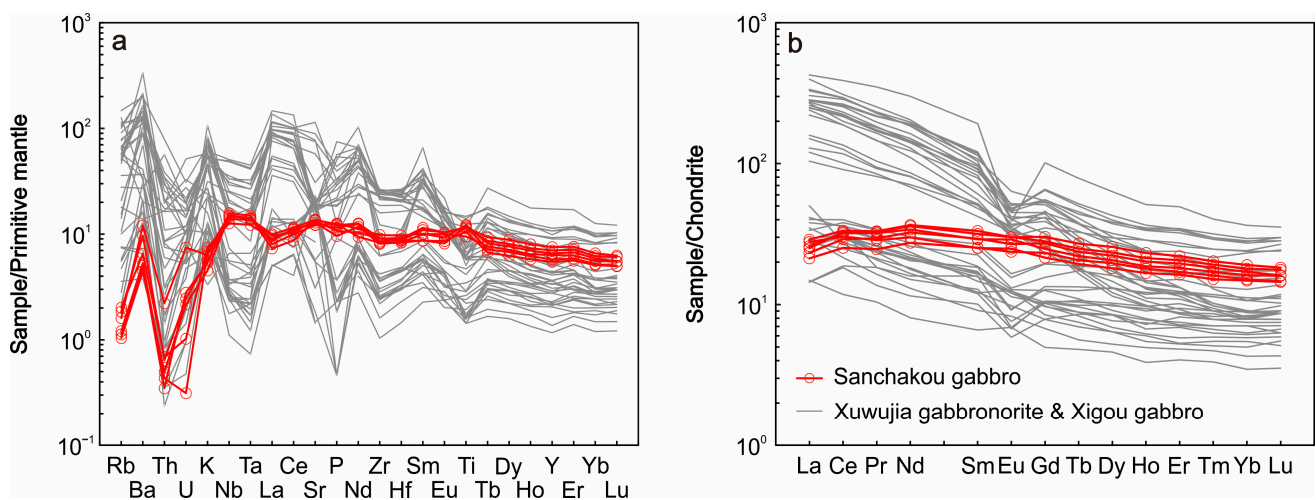


Figure 7. Chondrite-normalized REE (a) and primitive mantle-normalized trace element (b) patterns for the Sanchakou gabbros. The normalization values are from [79]. The trace elemental data of Xuwujia gabbronorites and Xigou gabbros are from [35].

Table 5. The whole-rock trace elemental data ($\times 10^{-6}$) of the Sanchakou gabbros.

Sample	SCK-1	SCK-2	SCK-3	SCK-4	SCK-5	SCK-6
Rb	1.28	1.17	0.77	0.72	1.02	0.66
Sr	271.97	282.96	258.95	257.62	289.98	287.52
Ba	45.74	67.76	37.23	35.06	84.33	31.27
Th	0.06	0.05	0.04	0.03	0.19	0.04
U	0.02	0.05	0.01	0.06	0.16	0.05
Zr	90.73	101.63	95.27	109.80	101.95	92.60
Hf	2.59	2.67	2.71	2.99	2.79	2.56
Nb	9.02	9.90	10.74	11.30	10.74	10.41
Ta	0.50	0.56	0.58	0.61	0.57	0.58
Sc	47.28	46.05	51.06	50.66	54.06	49.49
La	6.17	6.59	5.95	5.52	6.85	5.03
Ce	19.61	18.62	20.04	17.80	20.48	15.44
Pr	3.06	2.72	3.11	2.80	3.15	2.35
Nd	15.94	14.00	16.83	15.17	17.13	12.80
Sm	4.44	3.85	4.86	4.49	5.09	3.87
Eu	1.68	1.44	1.75	1.56	1.74	1.37
Gd	5.11	4.42	5.78	5.60	6.22	4.79
Tb	0.83	0.73	0.93	0.88	1.01	0.77
Dy	5.24	4.60	5.94	5.65	6.52	4.99
Ho	1.06	0.95	1.21	1.14	1.32	1.02
Er	3.01	2.70	3.42	3.24	3.65	2.82
Tm	0.44	0.39	0.49	0.47	0.52	0.41
Yb	2.75	2.51	3.06	2.90	3.25	2.57
Lu	0.41	0.37	0.45	0.41	0.46	0.37
Y	28.98	24.92	31.89	29.86	34.37	26.19
ΣREE	69.73	63.88	73.81	67.63	77.40	58.60
LREE/HREE	2.70	2.84	2.47	2.33	2.37	2.30
La _N /Yb _N	1.61	1.88	1.39	1.37	1.51	1.41
δEu	1.08	1.07	1.01	0.95	0.95	0.97
Sc/Y	1.63	1.85	1.60	1.70	1.57	1.89
Eu*/Eu	2.85	2.87	3.04	3.24	3.25	3.16
Sm/Yb	1.62	1.53	1.59	1.55	1.57	1.51
La/Yb	2.24	2.63	1.94	1.90	2.11	1.96
Th/Yb	0.02	0.02	0.01	0.01	0.06	0.02
TiO ₂ /Yb	0.75	0.91	0.80	0.92	0.77	1.01
La/Nb	0.68	0.67	0.55	0.49	0.64	0.48
La/Ba	0.13	0.10	0.16	0.16	0.08	0.16
Th/Yb	0.02	0.02	0.01	0.01	0.06	0.02
Ba/La	7.41	10.28	6.26	6.35	12.31	6.21
Ba/Th	782.96	1243.80	1008.25	1185.70	447.10	739.64
Th/Nb	0.01	0.01	0.00	0.00	0.02	0.00

4.3.3. Sr-Nd Isotopes

The whole-rock Sr-Nd isotopic data of the Sanchakou gabbros are listed in Table 6. The $^{87}\text{Sr}/^{86}\text{Sr}$ ratios range from 0.704313 to 0.704882, slightly higher than the mantle value (0.704) and lower than the average value of the continental crust (0.719). The calculated $(^{87}\text{Sr}/^{86}\text{Sr})_i$ ratios range from 0.703942 to 0.704702, lower than that of basaltic magma formed by mantle (0.706) and granite formed by partial melting of crust (0.718). The $^{143}\text{Nd}/^{144}\text{Nd}$ ratios range from 0.512364 to 0.512573, lower than the modern value of the primitive mantle (0.512638). The $\epsilon_{\text{Nd}}(t)$ values are all positive, ranging from 2.12 to 2.39. The Sm-Nd T_{DM} age ranges from 2535 Ma to 2834 Ma. The Sm-Nd $T_{\text{DM}2}$ age ranges from 2204 Ma to 2226 Ma. In the $\epsilon_{\text{Nd}}(t)$ - $(^{87}\text{Sr}/^{86}\text{Sr})_i$ diagram [80], the Sanchakou gabbros fall into the continental basalt or oceanic island basalt (OIB) field (Figure 8a).

Table 6. The whole-rock Sr-Nd isotopic data of the Sanchakou gabbros.

Sample	$^{87}\text{Rb}/^{86}\text{Sr}$	$^{87}\text{Sr}/^{86}\text{Sr}$	$\pm 1\sigma$	$(^{87}\text{Sr}/^{86}\text{Sr})_i$	$^{147}\text{Sm}/^{144}\text{Nd}$	$^{143}\text{Nd}/^{144}\text{Nd}$	$\pm 1\sigma$	$\epsilon_{\text{Nd}}(t)$	TDM (Ma)	TDM2 (Ma)
SCK-1	0.0136	0.704313	0.000005	0.703942	0.1684	0.512389	0.000002	2.12	2563	2226
SCK-2	0.0120	0.704346	0.000004	0.704019	0.1664	0.512364	0.000002	2.13	2535	2225
SCK-3	0.0086	0.704425	0.000005	0.704191	0.1743	0.512474	0.000002	2.33	2619	2209
SCK-4	0.0080	0.704634	0.000004	0.704415	0.1787	0.512528	0.000003	2.28	2716	2213
SCK-5	0.0102	0.704731	0.000005	0.704454	0.1797	0.512545	0.000002	2.39	2713	2204
SCK-6	0.0066	0.704882	0.000004	0.704702	0.1826	0.512573	0.000003	2.21	2834	2219

5. Discussion

5.1. Duration of Magmatism and UHT Metamorphism

The Paleoproterozoic Khondalite Belt is characterized by widespread UHT granulites/gneisses and large-scale magmatic events. Combined with previous studies in the Jining terrane, the results of zircon U-Pb geochronology analysis in UHT granulites/gneisses show the extensive and continuous “beaded” distribution along the concordia line, with an average age of ~ 1.92 Ga [30,31,44,50]. The occurrence time of UHT metamorphism is still controversial. One view is that it occurred at approximately ~ 1.92 Ga [52]. The other view is that it occurred before ~ 1.94 Ga, and then the rock experienced a slow cooling process of ~ 40 Myr [32]. However, it is generally believed that the cooling duration of UHT metamorphism varies with the tectonic environment. The slow cooling is usually >30 Myr, while the rapid cooling is mostly <10 Myr [81,82]. The “beaded” concordia diagram is more likely to reflect the slow cooling process [29,83–85]. Therefore, the UHT metamorphism in the Jining terrane belongs to the slow cooling and long-term persistent type, which is similar to that in the Rogaland area of Norway [84] and the Napier complex in East Antarctica [83]. Through the zircon U-Pb geochronology analysis of the Sanchakou gabbros, we found that the magmatism occurred from ~ 1.94 Ga to ~ 1.82 Ga, with a duration over 100 Ma and a peak time of ~ 1.94 Ga. It is coupled with the peak period and slow cooling process of UHT metamorphism in the Jining terrane. Therefore, the magma of these basic intrusive rocks may be the heat source for the UHT metamorphism [30,35,52,86].

5.2. Genesis of Layered Complex

In previous studies, the layered complex is always considered to be the magmatic product undergone a special process of fractional crystallization. In the closed magmatic system, the layered complex can be formed by the magmatic differentiation with only one large-scale magma injection and little or no magma replenishment, such as the Skaergaard complex in Greenland [87]. In the open magmatic system, the layered complex can be formed by magmatic differentiation after the multiple magma injection, such as the Muskox complex in Canada [88], the Bushveld complex in South Africa [89], the Stillwater complex in America [90], and the Rum complex in Britain [91]. However, the fractional crystallization process is usually accompanied by the contamination of crustal wallrocks in many cases [92,93]. Crustal contamination can change the compositions of magmatic melts [94,95]. Here, we discuss the genesis of the Sanchakou gabbros.

5.2.1. Crustal Contamination and Fractional Crystallization

We often regard “Assimilation and Fractional Crystallization (AFC)” as a significant process during the magmatic evolution, which can modify the geochemical compositions of the initial magma [94–96]. It does not probably occur in the shallow crust, because there is not enough energy accumulation [97]. The binary diagrams of $\epsilon_{\text{Nd}}(t)$, $\text{Mg}^\#$ versus SiO_2 show roughly negative correlations, indicating the Sanchakou gabbros are formed in the AFC process and similar to experimental results from peridotite melts (Figure 8b,c). The occurrence of the AFC process is supported by the 2225–2375 Ma inherited zircon in CL images. The $\text{Mg}^\#$ is often taken to reveal the process of fractional crystallization. There is a positive correlation between $\text{CaO}/\text{Al}_2\text{O}_3$ ratio and $\text{Mg}^\#$, further suggesting that the

clinopyroxene is probably the main fractionating mineral phase (Figure 8d). The Sc/Y ratio is usually controlled by clinopyroxene crystallization [98]. The decreasing Sc/Y ratio with the decreasing Mg[#] also indicates the crystallization of clinopyroxene (Figure 8e). The plagioclase does not play a vital role during the magmatic evolution, as shown by the nearly constant Eu^{*}/Eu with the decreasing Mg[#] (Figure 8f).

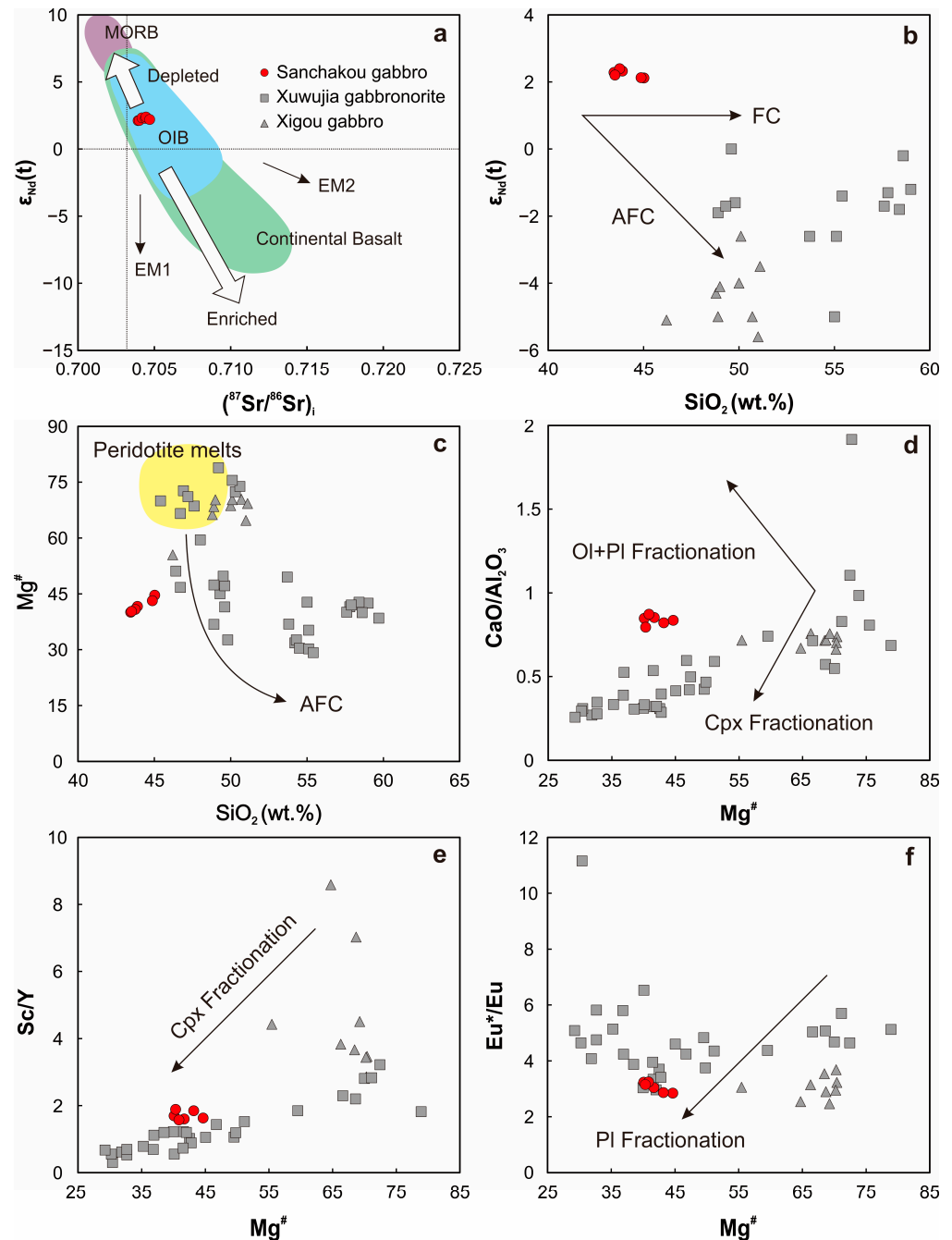


Figure 8. Geochemical diagrams of the Sanchakou gabbros. (a) The $\epsilon_{Nd}(t)$ versus I_{Sr} diagram (after [80]). (b) The $\epsilon_{Nd}(t)$ versus SiO_2 diagram. (c) The $Mg^\#$ versus SiO_2 diagram. Supposed peridotite melts and crust AFC curve are after [99]. (d) The CaO/Al_2O_3 versus $Mg^\#$ diagram. (e) The Sc/Y versus $Mg^\#$ diagram. (f) The Eu^*/Eu versus $Mg^\#$ diagram. Mineral abbreviations: Cpx, clinopyroxene; Ol, olivine; Pl, plagioclase. The major and trace elemental data of Xuwujia gabbrronites and Xigou gabbros are from [35].

5.2.2. Magmatic Source and Fluid Metasomatism

The Sr-Nd and Hf-O isotopic systems are used to determine the source of magmatic rocks. The Sanchakou gabbros have a positive whole-rock $\epsilon_{\text{Nd}}(t)$ value (2.12~2.39) and a negative zircon $\epsilon_{\text{Hf}}(t)$ value (-8.4~-3.8), reflecting the characteristics of Nd-Hf isotopic decoupling. The $\epsilon_{\text{Nd}}(t)$ -($^{87}\text{Sr}/^{86}\text{Sr}$)_i diagram [80] of Sanchakou gabbros indicates that the magma source may be a depleted mantle (Figure 8a). In the $\delta^{18}\text{O}$ - ϵ_{Hf} (Paleoproterozoic) diagram [100], most concordant zircons fall in the mixing line between the 3.5 Ga supracrustal component and the depleted mantle with Hf concentration ratios ($\text{Hf}_{\text{pm}}/\text{Hf}_{\text{c}}$) of 0.7 and 1.5 (Figure 9), indicating that the magma source may be enriched mantle or suffered from the crustal contamination [74]. In the process of mantle evolution, Nd and Hf are more likely to enter the melts than their parent isotopes, but the mobility of Nd is higher than that of Hf [101]. Lu-Hf isotope system is mainly controlled by Hf-rich minerals such as zircon, apatite, and garnet, and the Nd-Hf isotopic decoupling can occur during partial melting [102,103]. Due to the difference in partial melting conditions and the duration of magmatic events, it is difficult to achieve the isotopic equilibrium, resulting in the Nd-Hf isotopic decoupling between the melt and the source region [104]. However, the Sm-Nd T_{DM} age (2535~2834 Ma) and the Lu-Hf T_{DM} age (2444~2609 Ma) are in a similar range, which is older than the formation age of Sanchakou gabbros. Therefore, it is very likely that the Nd-Hf isotopic decoupling occurred during mantle-derived magma mixing with crustal wallrocks in the magma chamber.

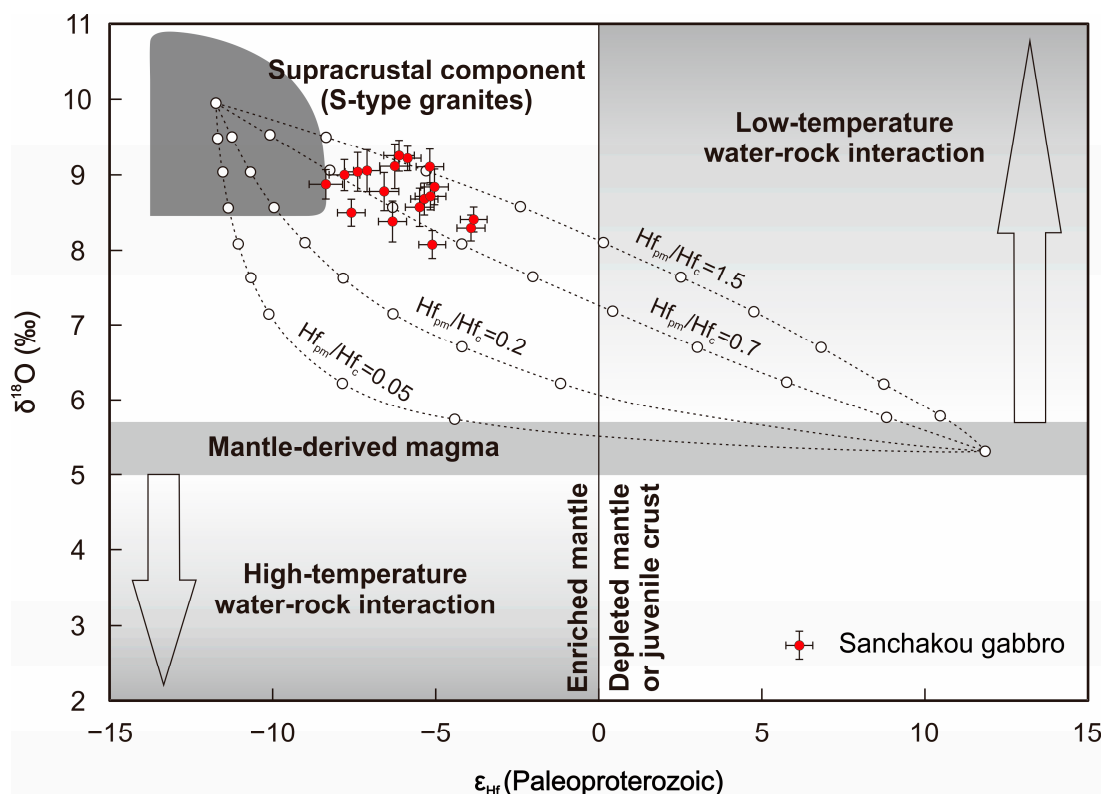


Figure 9. The zircon $\delta^{18}\text{O}$ versus $\epsilon_{\text{Hf}}(t)$ diagram of the Sanchakou gabbros. The dotted lines indicate the two-component mixing trends between the depleted mantle and the supracrust-derived magma. We assume that the supracrustal zircons have $\epsilon_{\text{Hf}}(t) = -12$ and $\delta^{18}\text{O} = 10\text{‰}$, the depleted mantle zircons have $\epsilon_{\text{Hf}}(t) = 12$ and $\delta^{18}\text{O} = 5.3\text{‰}$ [105]. $\text{Hf}_{\text{pm}}/\text{Hf}_{\text{c}}$ is the Hf concentration ratio between the parental mantle-derived magma and supracrustal components indicated for each curve. The small circles on the curves indicate 10% mixing increments. The zircon Hf-O isotope compositions of the supracrustal component (S-type granites) are from [105], and those of the depleted mantle are from [75].

The melting depths of the layered complex can be modeled with related trace elements [106,107]. REE ratios and abundances (e.g., Sm/Yb, and La/Yb and Sm) are widely used to determine the origin of magma and the melting degree of mantle [107–110]. The Sanchakou gabbros plot near the spinel + garnet lherzolite melting curves with primitive mantle (PM) starting compositions. The Sm/Yb ratios are lower than the garnet lherzolite melting curves and higher than the spinel lherzolite melting curves (Figure 10a,b). The parental magma is likely to be derived from a mantle source consisting of spinel + garnet lherzolite. Additionally, approximately 10%–20% partial melting of the lherzolites is required.

The Sanchakou gabbros have a relatively lower Th/Yb ratio and higher TiO₂/Yb ratio, and all of the points fall outside the MORB-OIB array (Figure 10c,d), similar to subduction-related enrichment [111]. All of the samples exhibit a relatively high La/Nb ratio (0.48–33.67) and low La/Ba ratio (0.01–0.16), derived from a similar modified continental lithospheric mantle (CLM) source [112]. The basic magma formed by the partial melting of mantle peridotite that has interacted with fluids usually has relatively high Na₂O and P₂O₅ contents, positive to weakly negative Nb anomalies, and non-negative Ti anomalies relative to the PM [113,114]. It is similar to the characteristics of Sanchakou gabbros, thus supporting the interaction between the CLM and the fluids.

The trace element ratios (e.g., Th/Yb, Ba/La, Ba/Th, and Th/Nb) are widely used to distinguish whether metasomatic agents belong to fluids or sediments [115,116]. All the samples have variable Ba/La (6.21–76.85) and Ba/Th (39.50–18,537.50) ratios but relatively constant Th/Yb (0.01–6.59) and Th/Nb (0.00–2.51) ratios (Figure 10e,f), which can be considered as the addition of fluids into the mantle source [116–118]. The highly variable Sr/Nd (2.40–127.39) ratio and relatively low Th/Yb (0.01–6.59) ratio further suggest that the fluids could be derived from the large-scale melting crust [119].

In summary, we believe that crustal contamination plays an important role in the formation of Sanchakou gabbros. The magma originates from the 10%–20% partial melting of the spinel + garnet lherzolite mantle. The Sanchakou gabbros are magmatic crystallization products mixed with crustal wallrocks in the magma chamber.

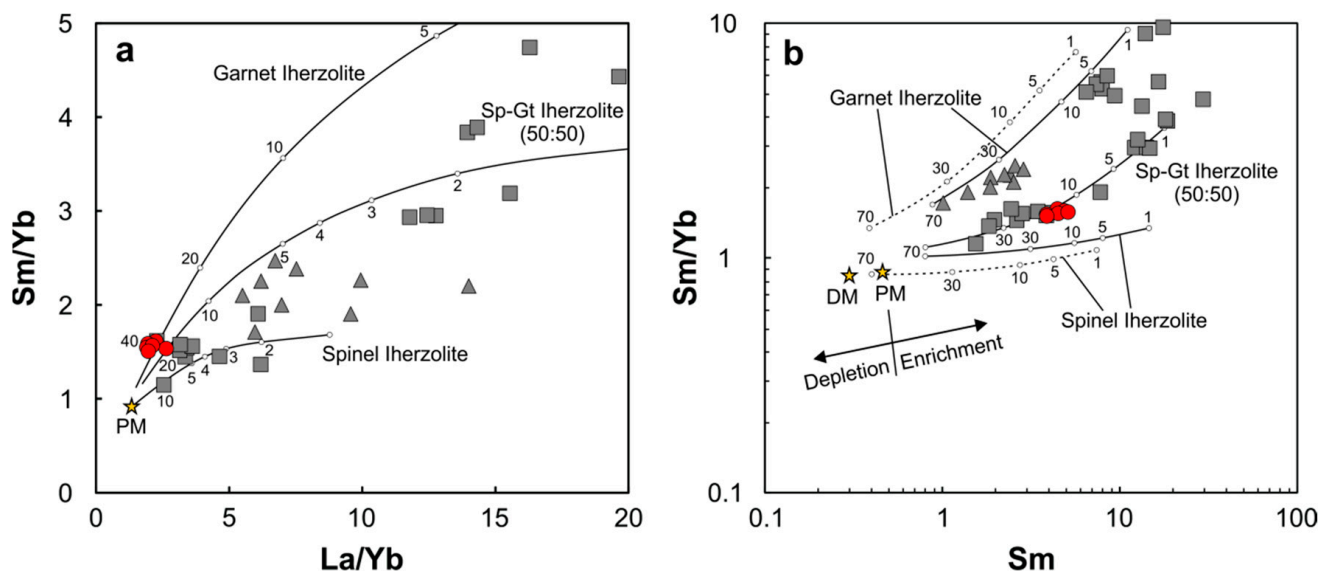


Figure 10. Cont.

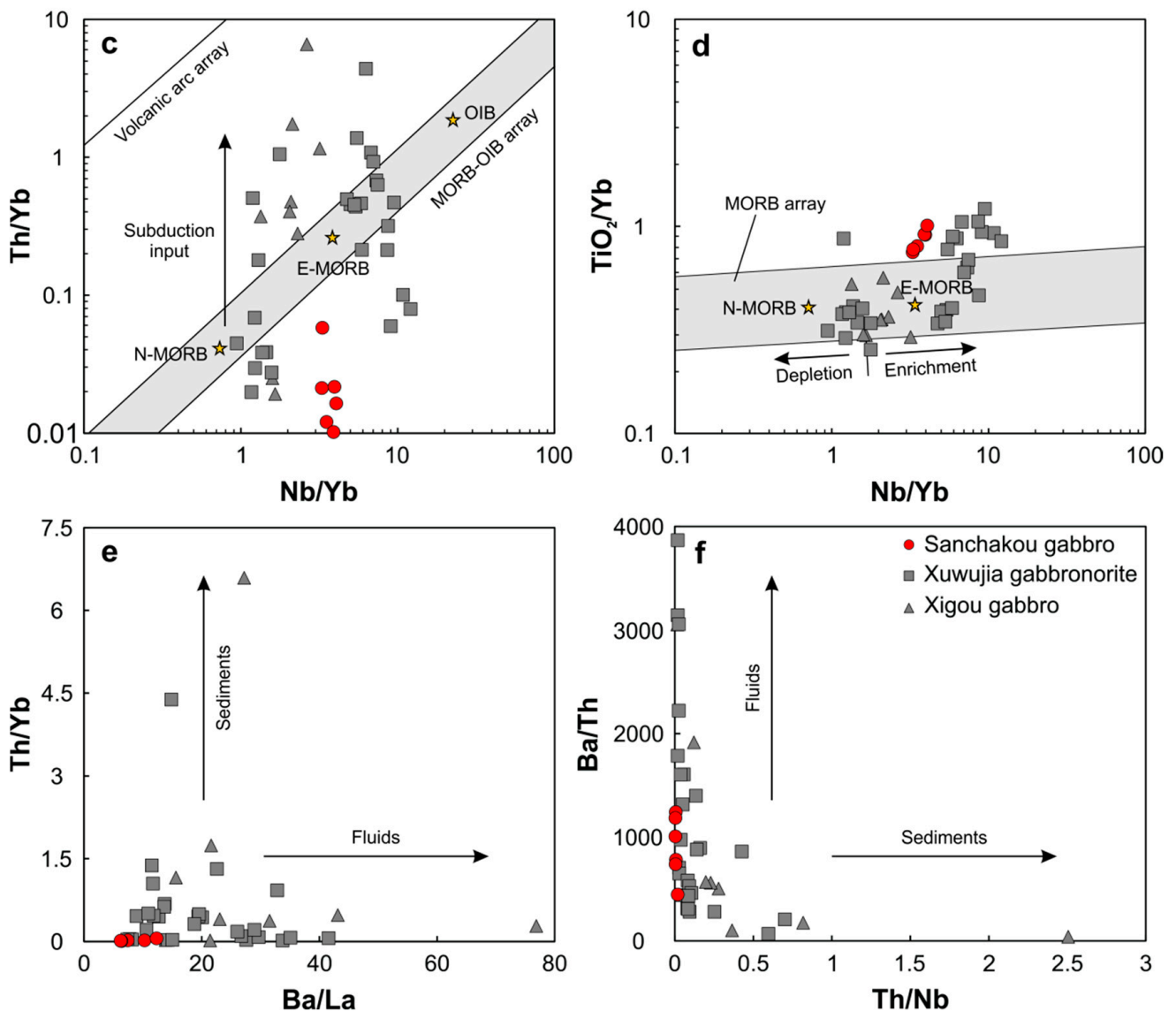


Figure 10. Geochemical diagrams of the Sanchakou gabbros. (a) The Sm/Yb versus La/Yb diagram (after [120]). (b) The Sm/Yb versus Sm diagram (after [107]). Solid and dashed curves are the melting trends from DM (depleted MORB) and PM (primitive mantle). (c) The Th/Yb versus Nb/Yb diagram (after [121]). (d) The TiO₂/Yb versus Nb/Yb diagram (after [121]). (e) The Th/Yb versus Ba/La diagram (after [116]). (f) The Ba/Th versus Th/Nb diagram (after [115]). The major and trace elemental data of Xuwujia gabbronorites and Xigou gabbros are from [35].

5.3. Tectonic Implications

It is generally believed that the Khondalite Belt is the tectonic amalgamation belt of the Ordos and Yinshan Blocks at ~1.95 Ga, which is a typical Paleoproterozoic continent-continent collisional belt [20,43]. This view is supported by the Precambrian granulites/gneisses, but it is still unclear whether it is consistent with the magmatic rocks. A few studies have focused on 2.45~2.10 Ga, 1.97~1.92 Ga, and 1.85~1.84 Ga basic intrusive rocks in the Jining terrane, indicating that they were involved in the subduction and collision processes during the formation of the Khondalite Belt [34–37]. However, the detailed tectonic environment is still controversial.

For the tectonic environment of Jining terrane at 1.95~1.82 Ga, researchers have proposed a variety of models, including mantle plume events [21], mid-ocean ridge subduction [22,35,86], and post-collision mantle upwelling [30,122]. The mid-ocean ridge subduc-

tion usually forms double metamorphic zones and adakitic rocks [123,124], which have not been found in the Jining terrane. The post-collision mantle upwelling model also seems to be insufficient, because the duration of UHT metamorphism formed under this condition is generally within ~30 Myr [81,82], and the upper-temperature limit is usually less than 1000 °C [125,126], which contradicts the fact that extremely high-temperature metamorphic rocks are exposed in the Jining terrane [32]. In addition, the back-arc basin has twice the heat flow value compared with the normal craton, which is also an ideal environment for UHT metamorphism [127,128]. The geothermal gradient is only 20~25 °C/km [127,129], and high-grade metamorphic rocks usually have anticlockwise P-T paths [82,130]. However, it is contrary to the fact that most UHT granulites/gneisses reported in the Jining terrane have clockwise P-T paths [20,43]. Combined with previous studies, the layered complex often forms in the tectonic environment associated with mantle plume or intracontinental rifting, such as the Stillwater complex, the Duluth complex in America, and the Muskox complex in Canada [10–13]. Only a few form in the late-orogenic or post-orogenic extensional environment, such as the Bjerkreim-Sokndal complex and the Fongen-Hyllingen complex in Norway [131,132]. For basic intrusive rocks in the Jining terrane, the magma emplacement temperature is as high as ~1400 °C, and the mantle potential temperature is about ~1550 °C [35] which is slightly higher than that of the Paleoproterozoic mantle (~1500 °C) [133–135]. It is probably caused by the upwelling asthenosphere. The duration of UHT metamorphism depends on the duration of asthenosphere upwelling.

Therefore, we produce a hypothetical tectonic framework for the Khondalite Belt to explain the tectonic evolution at 1.95~1.82 Ga. With the end of the amalgamation between the Ordos and Yinshan Blocks at ~1.95 Ga [20,43], the asthenosphere upwelling resulted in large-scale crustal melting and long-term magmatism. The magma assimilated crustal wallrocks, and then fractional crystallized to form the layered complex (Figure 11), in which several fluids of granulites/gneisses were mixed. Meanwhile, the surrounding granulites/gneisses were heated to form the UHT metamorphism.

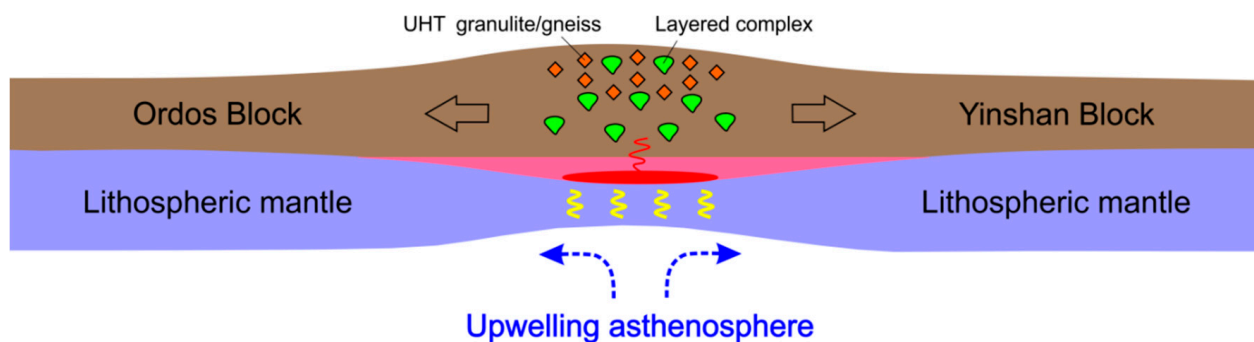


Figure 11. Cartoons showing the tectonic evolution of the Khondalite Belt between ~1.95 Ga and ~1.82 Ga.

6. Concluding Remarks

Based on the in situ zircon U-Pb isotopic analysis of the Sanchakou gabbros, we have found that they have experienced a slow cooling process from ~1.94 Ga to ~1.82 Ga, with a weighted average age of 1923 ± 28 Ma. Combined with the study of elemental and Hf-O-Sr-Nd isotopic analysis, we believe that they are the crystallization products of assimilating crustal wallrocks after 10%~20% partial melting of spinel + garnet lherzolite mantle, probably formed by the asthenosphere upwelling after the amalgamation of the Ordos and Yinshan Blocks.

Author Contributions: Conceptualization, W.-P.Z. and W.T.; methodology, W.-P.Z.; software, W.-P.Z.; validation, W.-P.Z., W.T. and B.W.; formal analysis, W.-P.Z.; investigation, W.-P.Z., Y.-H.Z. and C.-J.W.; resources, Y.-H.Z.; data curation, W.-P.Z. and W.T.; writing—original draft preparation, W.-P.Z.; writing—review and editing, W.T. and C.-J.W.; visualization, B.W.; supervision, W.T.; project administration, W.T.; funding acquisition, W.T., Y.-H.Z. and C.-J.W. All authors have read and agreed to the published version of the manuscript.

Funding: This research was funded by the National Natural Science Foundation of China (Grant No. 42030304, 42202047), the National Key Research & Development Program of China (Grant No. 2018YFE0204202, 2017YFC0601302), and the China Geological Survey (Grant No. DD20221649, DD20221647).

Data Availability Statement: Not applicable.

Acknowledgments: Constructive suggestions and comments from anonymous reviewers led to great improvements in the quality of this article.

Conflicts of Interest: The authors declare no conflict of interest.

References

1. Wager, L.R.; Brown, G.M. *Layered Igneous Rocks*; Oliver and Boyd: Edinburgh, UK; London, UK, 1968.
2. Hoatson, D.M.; Sun, S.S. Archean layered mafic-ultramafic intrusions in the West Pilbara Craton, Western Australia: A synthesis of some of the oldest orthomagmatic mineralizing systems in the world. *Econ. Geol.* **2002**, *97*, 847–872. [[CrossRef](#)]
3. Ripley, E.M.; Shafer, P.; Li, C.; Hauck, S.A. Re-Os and O isotopic variations in magnetite from the contact zone of the Duluth Complex and the Biwabik Iron Formation, northeastern Minnesota. *Chem. Geol.* **2008**, *249*, 213–226. [[CrossRef](#)]
4. Roelofse, F.; Ashwal, L.D. The Lower Main Zone in the Northern Limb of the Bushveld Complex—A >1.3 km thick sequence of intruded and variably contaminated crystal mushes. *J. Petrol.* **2012**, *53*, 1449–1476. [[CrossRef](#)]
5. Maier, W.D.; Halkoaho, T.; Huhma, H.; Hanski, E.; Barnes, S.J. The Penikat intrusion, Finland: Geochemistry, geochronology, and origin of platinum-palladium reefs. *J. Petrol.* **2018**, *59*, 967–1006. [[CrossRef](#)]
6. Wall, C.J.; Scoates, J.S.; Weis, D.; Friedman, R.M.; Amini, M.; Meurer, W.P. The Stillwater Complex: Integrating zircon geochronological and geochemical constraints on the age, emplacement history and crystallization of a large, open-system layered intrusion. *J. Petrol.* **2018**, *59*, 153–190. [[CrossRef](#)]
7. Zhou, M.F.; Arndt, N.T.; Malpas, J.; Wang, C.Y.; Kennedy, A.K. Two magma series and associated ore deposit types in the Permian Emeishan large igneous province, SW China. *Lithos* **2008**, *103*, 352–368. [[CrossRef](#)]
8. Zhong, H.; Campbell, I.H.; Zhu, W.G.; Allen, C.M.; Hu, R.Z.; Xie, L.W.; He, D.F. Timing and source constraints on the relationship between mafic and felsic intrusions in the Emeishan large igneous province. *Geochim. Cosmochim. Acta* **2011**, *75*, 1374–1395. [[CrossRef](#)]
9. Wotzlaw, J.F.; Bindeman, I.N.; Schaltegger, U.; Brooks, C.K.; Naslund, H.R. High-resolution insights into episodes of crystallization, hydrothermal alteration and remelting in the Skaergaard intrusive complex. *Earth Planet. Sci. Lett.* **2012**, *355*, 199–212. [[CrossRef](#)]
10. Nicholson, S.W.; Shirey, S.B. Midcontinent rift volcanism in the Lake Superior region: Sr, Nd, and Pb isotopic evidence for a mantle plume origin. *J. Geophys. Res. Solid Earth* **1990**, *95*, 10851–10868. [[CrossRef](#)]
11. Paces, J.B.; Miller, J.D., Jr. Precise U-Pb ages of Duluth complex and related mafic intrusions, northeastern Minnesota: Geochronological insights to physical, petrogenetic, paleomagnetic, and tectonomagmatic processes associated with the 1.1 Ga midcontinent rift system. *J. Geophys. Res. Solid Earth* **1993**, *98*, 13997–14013. [[CrossRef](#)]
12. Mackie, R.A.; Scoates, J.S.; Weis, D. Age and Nd-Hf isotopic constraints on the origin of marginal rocks from the Muskox layered intrusion (Nunavut, Canada) and implications for the evolution of the 1.27 Ga Mackenzie large igneous province. *Precambrian Res.* **2009**, *172*, 46–66. [[CrossRef](#)]
13. Bai, Y.; Su, B.X.; Xiao, Y.; Chen, C.; Cui, M.M.; He, X.Q.; Qin, L.P.; Charlier, B. Diffusion-driven chromium isotope fractionation in ultramafic cumulate minerals: Elemental and isotopic evidence from the Stillwater Complex. *Geochim. Cosmochim. Acta* **2019**, *263*, 167–181. [[CrossRef](#)]
14. Bowen, N.L. *The Evolution of Igneous Rocks*; Princeton University Press: Princeton, NJ, USA, 1928.
15. Reiners, P.W.; Nelson, B.K.; Ghiorso, M.S. Assimilation of felsic crust by basaltic magma: Thermal limits and extents of crustal contamination of mantle-derived magmas. *Geology* **1995**, *23*, 563–566. [[CrossRef](#)]
16. Anderson, A.T., Jr. Parental basalts in subduction zones: Implications for continental evolution. *J. Geophys. Res. Solid Earth* **1982**, *87*, 7047–7060. [[CrossRef](#)]
17. Taylor, S.R.; McLennan, S.M. The geochemical evolution of the continental crust. *Rev. Geophys.* **1995**, *33*, 241–265. [[CrossRef](#)]
18. Kuşçu, G.G.; Floyd, P.A. Mineral compositional and textural evidence for magma mingling in the Saraykent volcanics. *Lithos* **2001**, *56*, 207–230. [[CrossRef](#)]
19. Arvin, M.; Dargahi, S.; Babaei, A.A. Mafic microgranular enclave swarms in the Chenar granitoid stock, NW of Kerman, Iran: Evidence for magma mingling. *J. Asian Earth Sci.* **2004**, *24*, 105–113. [[CrossRef](#)]

20. Zhao, G.C.; Sun, M.; Wilde, S.A.; Li, S.Z. Late Archean to Paleoproterozoic evolution of the North China Craton: Key issues revisited. *Precambrian Res.* **2005**, *136*, 177–202. [[CrossRef](#)]
21. Santosh, M.; Tsunogae, T.; Ohyama, H.; Sato, K.; Li, J.H.; Liu, S.J. Carbonic metamorphism at ultrahigh-temperatures: Evidence from North China Craton. *Earth Planet. Sci. Lett.* **2008**, *266*, 149–165. [[CrossRef](#)]
22. Santosh, M.; Liu, S.J.; Tsunogae, T.; Li, J.H. Paleoproterozoic ultrahigh-temperature granulites in the North China Craton: Implications for tectonic models on extreme crustal metamorphism. *Precambrian Res.* **2012**, *223*, 77–106. [[CrossRef](#)]
23. Liu, S.J.; Li, J.H.; Santosh, M. First application of the revised Ti-in-zircon geothermometer to Paleoproterozoic ultrahigh-temperature granulites of Tuguiwula, Inner Mongolia, North China Craton. *Contrib. Mineral. Petrol.* **2010**, *159*, 225–235. [[CrossRef](#)]
24. Liu, S.J.; Xiang, B.; Li, J.H.; Santosh, M. Retrograde metamorphism of ultrahigh-temperature granulites from the Khondalite belt in Inner Mongolia, North China Craton: Evidence from aluminous orthopyroxenes. *Geol. J.* **2011**, *46*, 263–275. [[CrossRef](#)]
25. Liu, S.J.; Tsunogae, T.; Li, W.S.; Shimizu, H.; Santosh, M.; Wan, Y.S.; Li, J.H. Paleoproterozoic granulites from Helling'er: Implications for regional ultrahigh-temperature metamorphism in the North China Craton. *Lithos* **2012**, *148*, 54–70. [[CrossRef](#)]
26. Zhang, H.T.; Li, J.H.; Liu, S.J.; Li, W.S.; Santosh, M.; Wang, H.H. Spinel + quartz-bearing ultrahigh-temperature granulites from Xumayao, Inner Mongolia Suture Zone, North China Craton: Petrology, phase equilibria and counterclockwise P-T path. *Geosci. Front.* **2012**, *3*, 603–611. [[CrossRef](#)]
27. Cai, J.; Liu, F.L.; Liu, P.H.; Shi, J.R. Metamorphic P-T conditions and U-Pb dating of the sillimanite-cordierite-garnet paragneisses in Sanchakou, Jining area, Inner Mongolia. *Acta Petrol. Sin.* **2014**, *30*, 472–490. (In Chinese with English Abstract)
28. Yang, Q.Y.; Santosh, M.; Tsunogae, T. Ultrahigh-temperature metamorphism under isobaric heating: New evidence from the North China Craton. *J. Asian Earth Sci.* **2014**, *95*, 2–16. [[CrossRef](#)]
29. Li, X.W.; Wei, C.J. Phase equilibria modelling and zircon age dating of pelitic granulites in Zhaojiayao, from the Jining Group of the Khondalite Belt, North China Craton. *J. Metamorph. Geol.* **2016**, *34*, 595–615. [[CrossRef](#)]
30. Li, X.W.; Wei, C.J. Ultrahigh-temperature metamorphism in the Tuguiwula area, Khondalite Belt, North China Craton. *J. Metamorph. Geol.* **2018**, *36*, 489–509. [[CrossRef](#)]
31. Li, X.W.; White, R.W.; Wei, C.J. Can we extract ultrahigh-temperature conditions from Fe-rich metapelites? An example from the Khondalite Belt, North China Craton. *Lithos* **2019**, *328*, 228–243. [[CrossRef](#)]
32. Wang, B.; Wei, C.J.; Tian, W.; Fu, B. UHT metamorphism peaking above 1100 °C with slow cooling: Insights from pelitic granulites in the Jining complex, North China Craton. *J. Petrol.* **2020**, *61*, ega070. [[CrossRef](#)]
33. Cawthorn, R.G. *Layered Intrusions*; Elsevier Science: Amsterdam, The Netherlands, 1996.
34. Guo, J.H.; Shi, X.; Bian, A.G.; Xu, R.H.; Zhai, M.G.; Li, Y.G. Pb isotopic composition of feldspar and U-Pb age of zircon from early Proterozoic granite in Sanggan area, North China Craton: Metamorphism, crustal melting and tectono-thermal event. *Acta Petrol. Sin.* **1999**, *15*, 199–207. (In Chinese with English Abstract)
35. Peng, P.; Guo, J.H.; Zhai, M.G.; Bleeker, W. Paleoproterozoic gabbro-noritic and granitic magmatism in the northern margin of the North China Craton: Evidence of crust-mantle interaction. *Precambrian Res.* **2010**, *183*, 635–659. [[CrossRef](#)]
36. Wan, Y.S.; Xu, Z.Y.; Dong, C.Y.; Nutman, A.P.; Ma, M.; Xie, H.; Cu, H. Episodic Paleoproterozoic (~2.45, ~1.95 and ~1.85 Ga) mafic magmatism and associated high temperature metamorphism in the Daqingshan area, North China Craton: SHRIMP zircon U-Pb dating and whole-rock geochemistry. *Precambrian Res.* **2013**, *224*, 71–93. [[CrossRef](#)]
37. Liu, P.H.; Liu, F.L.; Liu, C.H.; Liu, J.H.; Wang, F.; Xiao, L.; Shi, J. Multiple mafic magmatic and high-grade metamorphic events revealed by zircons from meta-mafic rocks in the Daqingshan-Wulashan Complex of the Khondalite Belt, North China Craton. *Precambrian Res.* **2014**, *246*, 334–357. [[CrossRef](#)]
38. Liu, D.Y.; Nutman, A.P.; Compston, W.; Wu, J.S.; Shen, Q.H. Remnants of ≥ 3800 Ma crust in the Chinese part of the Sino-Korean craton. *Geology* **1992**, *20*, 339–342. [[CrossRef](#)]
39. Song, B.; Nutman, A.P.; Liu, D.; Wu, J. 3800 to 2500 Ma crustal evolution in the Anshan area of Liaoning Province, northeastern China. *Precambrian Res.* **1996**, *78*, 79–94. [[CrossRef](#)]
40. Wu, F.Y.; Zhang, Y.B.; Yang, J.H.; Xie, L.W.; Yang, Y.H. Zircon U-Pb and Hf isotopic constraints on the Early Archean crustal evolution in Anshan of the North China Craton. *Precambrian Res.* **2008**, *167*, 339–362. [[CrossRef](#)]
41. Zhai, M.G.; Santosh, M. The early Precambrian odyssey of the North China Craton: A synoptic overview. *Gondwana Res.* **2011**, *20*, 6–25. [[CrossRef](#)]
42. Kusky, T.M.; Polat, A.; Windley, B.F.; Burke, K.C.; Dewey, J.F.; Kidd, W.S.F.; Maruyama, S.; Wang, J.P.; Deng, H.; Wang, Z.S.; et al. Insights into the tectonic evolution of the North China Craton through comparative tectonic analysis: A record of outward growth of Precambrian continents. *Earth-Sci. Rev.* **2016**, *162*, 387–432. [[CrossRef](#)]
43. Zhao, G.C.; Cawood, P.A.; Li, S.Z.; Wilde, S.A.; Sun, M.; Zhang, J.; He, Y.H.; Yin, C.Q. Amalgamation of the North China Craton: Key issues and discussion. *Precambrian Res.* **2012**, *222*, 55–76. [[CrossRef](#)]
44. Santosh, M.; Wilde, S.A.; Li, J.H. Timing of Paleoproterozoic ultrahigh-temperature metamorphism in the North China Craton: Evidence from SHRIMP U-Pb zircon geochronology. *Precambrian Res.* **2007**, *159*, 178–196. [[CrossRef](#)]
45. Santosh, M.; Tsunogae, T.; Li, J.H.; Liu, S.J. Discovery of sapphirine-bearing Mg-Al granulites in the North China Craton: Implications for Paleoproterozoic ultrahigh temperature metamorphism. *Gondwana Res.* **2007**, *11*, 263–285. [[CrossRef](#)]
46. Santosh, M.; Sajeev, K.; Li, J.H.; Liu, S.J.; Itaya, T. Counterclockwise exhumation of a hot orogen: The Paleoproterozoic ultrahigh-temperature granulites in the North China Craton. *Lithos* **2009**, *110*, 140–152. [[CrossRef](#)]

47. Jiao, S.J.; Guo, J.H. Application of the two-feldspar geothermometer to ultrahigh-temperature (UHT) rocks in the Khondalite Belt, North China Craton and its implications. *Am. Mineral.* **2011**, *96*, 250–260. [[CrossRef](#)]
48. Jiao, S.J.; Guo, J.H.; Qian, M.; Zhao, R. Application of Zr-in-rutile thermometry: A case study from ultrahigh-temperature granulites of the Khondalite belt, North China Craton. *Contrib. Mineral. Petrol.* **2011**, *162*, 379–393. [[CrossRef](#)]
49. Shimizu, H.; Tsunogae, T.; Santosh, M.; Liu, S.J.; Li, J.H. Phase equilibrium modelling of Palaeoproterozoic ultrahigh temperature sapphirine granulite from the Inner Mongolia suture zone, North China Craton: Implications for counterclockwise P-T path. *Geol. J.* **2013**, *48*, 456–466. [[CrossRef](#)]
50. Lobjoie, C.; Wei, L.; Trap, P.; Goncalves, P.; Li, Q.; Marquer, D.; Devoir, A. Ultra-high temperature metamorphism recorded in Fe-rich olivine-bearing migmatite from the Khondalite belt, North China Craton. *J. Metamorph. Geol.* **2018**, *36*, 343–368. [[CrossRef](#)]
51. Wang, L.J.; Guo, J.H.; Yin, C.Q.; Peng, P.; Zhang, J.; Spencer, C.J.; Qian, J.H. High-temperature S-type granitoids (charnockites) in the Jining complex, North China Craton: Restite entrainment and hybridization with mafic magma. *Lithos* **2018**, *320*, 435–453. [[CrossRef](#)]
52. Huang, G.Y.; Guo, J.H.; Jiao, S.J.; Palin, R.M. What drives the continental crust to be extremely hot so quickly? *J. Geophys. Res. Solid Earth* **2019**, *124*, 11218–11231. [[CrossRef](#)]
53. Li, X.L.; Zhang, L.F.; Wei, C.J.; Slabunov, A.I.; Bader, T. Quartz and orthopyroxene exsolution lamellae in clinopyroxene and the metamorphic P-T path of Belomorian eclogites. *J. Metamorph. Geol.* **2018**, *36*, 1–12. [[CrossRef](#)]
54. Zong, K.Q.; Klemd, R.; Yuan, Y.; He, Z.Y.; Guo, J.L.; Shi, X.L.; Liu, Y.S.; Hu, Z.C.; Zhang, Z.M. The assembly of Rodinia: The correlation of early Neoproterozoic (ca. 900 Ma) high-grade metamorphism and continental arc formation in the southern Beishan Orogen, southern Central Asian Orogenic Belt (CAOB). *Precambrian Res.* **2017**, *290*, 32–48. [[CrossRef](#)]
55. Hu, Z.C.; Zhang, W.; Liu, Y.S.; Gao, S.; Li, M.; Zong, K.Q.; Chen, H.H.; Hu, S.H. “Wave” signal-smoothing and mercury-removing device for laser ablation quadrupole and multiple collector ICPMS analysis: Application to lead isotope analysis. *Anal. Chem.* **2015**, *87*, 1152–1157. [[CrossRef](#)]
56. Liu, Y.S.; Hu, Z.C.; Gao, S.; Günther, D.; Xu, J.; Gao, C.G.; Chen, H.H. In situ analysis of major and trace elements of anhydrous minerals by LA-ICP-MS without applying an internal standard. *Chem. Geol.* **2008**, *257*, 34–43. [[CrossRef](#)]
57. Liu, Y.S.; Gao, S.; Hu, Z.C.; Gao, C.G.; Zong, K.Q.; Wang, D.B. Continental and oceanic crust recycling-induced melt-peridotite interactions in the Trans-North China Orogen: U-Pb dating, Hf isotopes and trace elements in zircons of mantle xenoliths. *J. Petrol.* **2010**, *51*, 537–571. [[CrossRef](#)]
58. Ludwig, K.R. *ISOPLOT 3.00: A Geochronological Toolkit for Microsoft Excel*; Berkeley Geochronology Center: Berkeley, CA, USA, 2003; p. 39.
59. Jochum, K.P.; Nohl, U. Reference materials in geochemistry and environmental research and the GeoReM database. *Chem. Geol.* **2008**, *253*, 50–53. [[CrossRef](#)]
60. Chen, S.; Wang, X.H.; Niu, Y.L.; Sun, P.; Duan, M.; Xiao, Y.Y.; Guo, P.Y.; Gong, H.M.; Wang, G.D.; Xue, Q.Q. Simple and cost-effective methods for precise analysis of trace element abundances in geological materials with ICP-MS. *Sci. Bull.* **2017**, *62*, 277–289. [[CrossRef](#)] [[PubMed](#)]
61. Hu, Z.C.; Liu, Y.S.; Gao, S.; Liu, W.; Yang, L.; Zhang, W.; Tong, X.; Lin, L.; Zong, K.Q.; Li, M.; et al. Improved in situ Hf isotope ratio analysis of zircon using newly designed X skimmer cone and Jet sample cone in combination with the addition of nitrogen by laser ablation multiple collector ICP-MS. *J. Anal. At. Spectrom.* **2012**, *27*, 1391–1399. [[CrossRef](#)]
62. Woodhead, J.; Hergt, J.; Shelley, M.; Eggins, S.; Kemp, R. Zircon Hf-isotope analysis with an excimer laser, depth profiling, ablation of complex geometries, and concomitant age estimation. *Chem. Geol.* **2004**, *209*, 121–135. [[CrossRef](#)]
63. Zhang, W.; Hu, Z.C. Estimation of isotopic reference values for pure materials and geological reference materials. *At. Spectrosc.* **2020**, *41*, 93–102. [[CrossRef](#)]
64. Ickert, R.B.; Hiess, J.; Williams, I.S.; Holden, P.; Ireland, T.R.; Lanc, P.; Schram, N.; Foster, J.J.; Clement, S.W. Determining high precision, in situ, oxygen isotope ratios with a SHRIMP II: Analyses of MPI-DING silicate-glass reference materials and zircon from contrasting granites. *Chem. Geol.* **2008**, *257*, 114–128. [[CrossRef](#)]
65. Dong, C.Y.; Wan, Y.S.; Long, T.; Zhang, Y.H.; Liu, J.H.; Ma, M.Z.; Xie, H.Q.; Liu, D.Y. Oxygen isotopic compositions of zircons from Paleoproterozoic metasedimentary rocks in the Daqingshan-Jining area, North China Craton: In situ SHRIMP analysis. *Acta Petrol. Sin.* **2016**, *32*, 659–681. (In Chinese with English Abstract)
66. Black, L.P.; Kamo, S.L.; Allen, C.M.; Davis, D.W.; Aleinikoff, J.N.; Valley, J.W.; Mundil, R.; Campbell, I.H.; Korsch, R.J.; Williams, I.S.; et al. Improved ²⁰⁶Pb/²³⁸U microprobe geochronology by the monitoring of a trace-element-related matrix effect; SHRIMP, ID-TIMS, ELA-ICP-MS and oxygen isotope documentation for a series of zircon standards. *Chem. Geol.* **2004**, *205*, 115–140. [[CrossRef](#)]
67. Wiedenbeck, M.; Hanchar, J.M.; Peck, W.H.; Sylvester, P.; Valley, J.; Whitehouse, M.; Kronz, A.; Morishita, Y.; Nasdala, L.; Fiebig, J.; et al. Further Characterisation of the 91500 Zircon Crystal. *Geostand. Geoanal. Res.* **2004**, *28*, 9–39. [[CrossRef](#)]
68. Pin, C.; Gannoun, A.; Dupont, A. Rapid, simultaneous separation of Sr, Pb, and Nd by extraction chromatography prior to isotope ratios determination by TIMS and MC-ICP-MS. *J. Anal. At. Spectrom.* **2014**, *29*, 1858–1870. [[CrossRef](#)]
69. Pu, W.; Gao, J.F.; Zhao, K.D.; Ling, H.F.; Jiang, S.Y. Separation method of Rb-Sr, Sm-Nd using DCTA and HIBA. *J. Nanjing Univ. (Nat. Sci.)* **2005**, *41*, 445–450. (In Chinese with English Abstract)

70. Weis, D.; Kieffer, B.; Maerschalk, C.; Barling, J.; De Jong, J.; Williams, G.A.; Hanano, D.; Pretorius, W.; Mattielli, N.; Scoates, J.S.; et al. High-precision isotopic characterization of USGS reference materials by TIMS and MC-ICP-MS. *Geochem. Geophys. Geosystems* **2006**, *7*. [[CrossRef](#)]
71. Morimoto, N. Nomenclature of pyroxenes. *Mineral. Petrol.* **1988**, *39*, 55–76. [[CrossRef](#)]
72. Leake, B.E.; Woolley, A.R.; Birch, W.D.; Burke, E.A.; Ferraris, G.; Grice, J.D.; Hawthorne, F.C.; Kato, A.; Kisch, H.J.; Krivovichev, V.G.; et al. Nomenclature of amphiboles: Additions and revisions to the International Mineralogical Association's amphibole nomenclature. *Mineral. Mag.* **2004**, *68*, 209–215. [[CrossRef](#)]
73. Smith, J.V. I. Crystal Structure and Physical Properties. II. Chemical and Textural Properties. In *Feldspar Minerals*; Springer: Berlin/Heidelberg, Germany; New York, NY, USA, 1974; pp. 627, 690.
74. Wu, F.Y.; Li, X.H.; Zheng, Y.F.; Gao, S. Lu-Hf isotopic systematics and their applications in petrology. *Acta Petrol. Sin.* **2007**, *23*, 185–220. (In Chinese with English Abstract)
75. Valley, J.W.; Lackey, J.S.; Cavosie, A.J.; Clechenko, C.C.; Spicuzza, M.J.; Basei, M.A.S.; Bindeman, I.N.; Ferreira, V.P.; Sial, A.N.; King, E.M. 4.4 billion years of crustal maturation: Oxygen isotope ratios of magmatic zircon. *Contrib. Mineral. Petrol.* **2005**, *150*, 561–580. [[CrossRef](#)]
76. Wang, Z.; Wang, H.C.; Shi, J.R.; Chang, Q.S.; Zhang, J.H.; Ren, Y.W.; Xiang, Z.Q. Tectonic setting and geological significance of Xuwujia metagabbro in Jining area, Inner Mongolia. *Geol. Surv. Res.* **2020**, *43*, 97–113. (In Chinese with English Abstract)
77. Middlemost, E.A. Naming materials in the magma/igneous rock system. *Earth-Sci. Rev.* **1994**, *37*, 215–224. [[CrossRef](#)]
78. Rickwood, P.C. Boundary lines within petrologic diagrams which use oxides of major and minor elements. *Lithos* **1989**, *22*, 247–263. [[CrossRef](#)]
79. Sun, S.S.; McDonough, W.F. Chemical and isotopic systematics of oceanic basalts: Implications for mantle composition and processes. *Geol. Soc. Lond. Spec. Publ.* **1989**, *42*, 313–345. [[CrossRef](#)]
80. Zindler, A.; Hart, S. Chemical geodynamics. *Annu. Rev. Earth Planet. Sci.* **1986**, *14*, 493–571. [[CrossRef](#)]
81. Kelsey, D.E.; Hand, M. On ultrahigh temperature crustal metamorphism: Phase equilibria, trace element thermometry, bulk composition, heat sources, timescales and tectonic settings. *Geosci. Front.* **2015**, *6*, 311–356. [[CrossRef](#)]
82. Harley, S.L. A matter of time: The importance of the duration of UHT metamorphism. *J. Mineral. Petrol.* **2016**, *111*, 50–72. [[CrossRef](#)]
83. Clark, C.; Taylor, R.J.M.; Kylander-Clark, A.R.C.; Hacker, B.R. Prolonged (>100 Ma) ultrahigh temperature metamorphism in the Napier Complex, East Antarctica: A petrochronological investigation of Earth's hottest crust. *J. Metamorph. Geol.* **2018**, *36*, 1117–1139. [[CrossRef](#)]
84. Laurent, A.T.; Bingen, B.; Duchene, S.; Whitehouse, M.J.; Seydoux-Guillaume, A.M.; Bosse, V. Decoding a protracted zircon geochronological record in ultrahigh temperature granulite, and persistence of partial melting in the crust, Rogaland, Norway. *Contrib. Mineral. Petrol.* **2018**, *173*, 29. [[CrossRef](#)]
85. Jiao, S.J.; Guo, J.H.; Evans, N.J.; McDonald, B.J.; Liu, P.; Ouyang, D.J.; Fitzsimons, I.C.W. The timing and duration of high-temperature to ultrahigh-temperature metamorphism constrained by zircon U-Pb-Hf and trace element signatures in the Khondalite Belt, North China Craton. *Contrib. Mineral. Petrol.* **2020**, *175*, 66. [[CrossRef](#)]
86. Guo, J.H.; Peng, P.; Chen, Y.; Jiao, S.J.; Windley, B.F. UHT sapphirine granulite metamorphism at 1.93–1.92 Ga caused by gabbro intrusions: Implications for tectonic evolution of the northern margin of the North China Craton. *Precambrian Res.* **2012**, *222*, 124–142. [[CrossRef](#)]
87. Stewart, B.W.; DePaolo, D.J. Isotopic studies of processes in mafic magma chambers: II. The Skaergaard Intrusion, East Greenland. *Contrib. Mineral. Petrol.* **1990**, *104*, 125–141. [[CrossRef](#)]
88. Irvine, T.N. Crystallization sequences in the Muskox intrusion and other layered intrusions—II. Origin of chromitite layers and similar deposits of other magmatic ores. *Geochim. Cosmochim. Acta* **1976**, *39*, 991–1020. [[CrossRef](#)]
89. Kruger, F.J.; Marsh, J.S. Significance of ⁸⁷Sr/⁸⁶Sr ratios in the Merensky cyclic unit of the Bushveld Complex. *Nature* **1982**, *298*, 53–55. [[CrossRef](#)]
90. Irvine, T.N.; Keith, D.W.; Todd, S.G. The JM platinum-palladium reef of the Stillwater Complex, Montana; II, Origin by double-diffusive convective magma mixing and implications for the Bushveld Complex. *Econ. Geol.* **1983**, *78*, 1287–1334. [[CrossRef](#)]
91. Palacz, Z.A. Isotopic and geochemical evidence for the evolution of a cyclic unit in the Rhum intrusion, north-west Scotland. *Nature* **1984**, *307*, 618–620. [[CrossRef](#)]
92. Palacz, Z.A. Sr-Nd-Pb isotopic evidence for crustal contamination in the Rhum intrusion. *Earth Planet. Sci. Lett.* **1985**, *74*, 35–44. [[CrossRef](#)]
93. Ripley, E.M.; Lambert, D.D.; Frick, L.R. Re-Os, Sm-Nd, and Pb isotopic constraints on mantle and crustal contributions to magmatic sulfide mineralization in the Duluth Complex. *Geochim. Cosmochim. Acta* **1998**, *62*, 3349–3365. [[CrossRef](#)]
94. DePaolo, D.J. Trace element and isotopic effects of combined wallrock assimilation and fractional crystallization. *Earth Planet. Sci. Lett.* **1981**, *53*, 189–202. [[CrossRef](#)]
95. Halama, R.; Marks, M.; Brüggemann, G.; Siebel, W.; Wenzel, T.; Markl, G. Crustal contamination of mafic magmas: Evidence from a petrological, geochemical and Sr-Nd-Os-O isotopic study of the Proterozoic Isortoq dike swarm, South Greenland. *Lithos* **2004**, *74*, 199–232. [[CrossRef](#)]
96. Mir, A.R.; Alvi, S.H.; Balaram, V. Geochemistry of the mafic dykes in parts of the Singhbhum granitoid complex: Petrogenesis and tectonic setting. *Arab. J. Geosci.* **2011**, *4*, 933–943. [[CrossRef](#)]

97. Scarrow, J.H.; Leat, P.T.; Wareham, C.D.; Millar, I.L. Geochemistry of mafic dykes in the Antarctic Peninsula continental-margin batholith: A record of arc evolution. *Contrib. Mineral. Petrol.* **1998**, *131*, 289–305.
98. Naumann, T.R.; Geist, D.J. Generation of alkalic basalt by crystal fractionation of tholeiitic magma. *Geology* **1999**, *27*, 423–426. [[CrossRef](#)]
99. Stern, C.R.; Kilian, R. Role of the subducted slab, mantle wedge and continental crust in the generation of adakites from the Andean Austral Volcanic Zone. *Contrib. Mineral. Petrol.* **1996**, *123*, 263–281. [[CrossRef](#)]
100. Zhang, H.F.; Wang, J.L.; Zhou, D.W.; Yang, Y.H.; Zhang, G.W.; Santosh, M.; Yu, H.; Zhang, J. Hadean to Neoproterozoic episodic crustal growth: Detrital zircon records in Paleoproterozoic quartzites from the southern North China Craton. *Precambrian Res.* **2014**, *254*, 245–257. [[CrossRef](#)]
101. Yu, Y.; Huang, X.L.; Sun, M.; Yuan, C. Missing Sr-Nd isotopic decoupling in subduction zone: Decoding the multi-stage dehydration and melting of subducted slab in the Chinese Altai. *Lithos* **2020**, *362*, 105465. [[CrossRef](#)]
102. White, W.M. *Geochemistry*; John Wiley & Sons Inc.: Hoboken, NJ, USA, 2013.
103. Chen, Y.X.; Gao, P.; Zheng, Y.F. The anatectic effect on the zircon Hf isotope composition of migmatites and associated granites. *Lithos* **2015**, *238*, 174–184. [[CrossRef](#)]
104. Davies, G.R.; Tommasini, S. Isotopic disequilibrium during rapid crustal anatexis: Implications for petrogenetic studies of magmatic processes. *Chem. Geol.* **2000**, *162*, 169–191. [[CrossRef](#)]
105. Li, X.H.; Li, W.X.; Wang, X.C.; Li, Q.L.; Liu, Y.; Tang, G.Q. Role of mantle-derived magma in genesis of early Yanshanian granites in the Nanling Range, South China: In situ zircon Hf-O isotopic constraints. *Sci. China (Ser. D) Earth Sci.* **2009**, *52*, 1262–1278. [[CrossRef](#)]
106. Ellam, R.M. Lithospheric thickness as a control on basalt geochemistry. *Geology* **1992**, *20*, 153–156. [[CrossRef](#)]
107. Aldanmaz, E.R.C.A.N.; Pearce, J.A.; Thirlwall, M.F.; Mitchell, J.G. Petrogenetic evolution of late Cenozoic, post-collision volcanism in western Anatolia, Turkey. *J. Volcanol. Geotherm. Res.* **2000**, *102*, 67–95. [[CrossRef](#)]
108. McKenzie, D.A.N.; Bickle, M.J. The volume and composition of melt generated by extension of the lithosphere. *J. Petrol.* **1988**, *29*, 625–679. [[CrossRef](#)]
109. McKenzie, D.A.N.; O’Nions, R.K. Partial melt distributions from inversion of rare earth element concentrations. *J. Petrol.* **1991**, *32*, 1021–1091. [[CrossRef](#)]
110. Su, Y.; Zheng, J.; Griffin, W.L.; Zhao, J.; Tang, H.; Ma, Q.; Lin, X. Geochemistry and geochronology of Carboniferous volcanic rocks in the eastern Junggar terrane, NW China: Implication for a tectonic transition. *Gondwana Res.* **2012**, *22*, 1009–1029. [[CrossRef](#)]
111. Pearce, J.A.; Peate, D.W. Tectonic implications of the composition of volcanic arc magmas. *Annu. Rev. Earth Planet. Sci.* **1995**, *23*, 251–285. [[CrossRef](#)]
112. Saunders, A.D.; Storey, M.; Kent, R.W.; Norry, M.J. Consequences of plume-lithosphere interactions. *Geol. Soc. Lond. Spec. Publ.* **1992**, *68*, 41–60. [[CrossRef](#)]
113. Sajona, F.G.; Maury, R.C.; Pubellier, M.; Leterrier, J.; Bellon, H.; Cotten, J. Magmatic source enrichment by slab-derived melts in a young post-collision setting, central Mindanao (Philippines). *Lithos* **2000**, *54*, 173–206. [[CrossRef](#)]
114. Wang, Q.; Zhao, Z.H.; Bai, Z.H.; Bao, Z.W.; Xiong, X.L.; Mei, H.J.; Xu, J.F.; Wang, Y.X. Carboniferous adakites and Nb-enriched arc basaltic rocks association in the Alataw Mountains, north Xinjiang: Interactions between slab melt and mantle peridotite and implications for crustal growth. *Chin. Sci. Bull.* **2003**, *48*, 2108–2115. [[CrossRef](#)]
115. Hawkesworth, C.J.; Turner, S.P.; McDermott, F.; Peate, D.W.; Van Calsteren, P. U-Th isotopes in arc magmas: Implications for element transfer from the subducted crust. *Science* **1997**, *276*, 551–555. [[CrossRef](#)]
116. Woodhead, J.D.; Hergt, J.M.; Davidson, J.P.; Eggins, S.M. Hafnium isotope evidence for ‘conservative’ element mobility during subduction zone processes. *Earth Planet. Sci. Lett.* **2001**, *192*, 331–346. [[CrossRef](#)]
117. Hanyu, T.; Tatsumi, Y.; Nakai, S.I.; Chang, Q.; Miyazaki, T.; Sato, K.; Tani, K.; Shibata, T.; Yoshida, T. Contribution of slab melting and slab dehydration to magmatism in the NE Japan arc for the last 25 Myr: Constraints from geochemistry. *Geochem. Geophys. Geosystems* **2006**, *7*. [[CrossRef](#)]
118. Tian, L.Y.; Castillo, P.R.; Hilton, D.R.; Hawkins, J.W.; Hanan, B.B.; Pietruszka, A.J. Major and trace element and Sr-Nd isotope signatures of the northern Lau Basin lavas: Implications for the composition and dynamics of the back-arc basin mantle. *J. Geophys. Res. Solid Earth* **2011**, *116*. [[CrossRef](#)]
119. Woodhead, J.D.; Eggins, S.M.; Johnson, R.W. Magma genesis in the New Britain island arc: Further insights into melting and mass transfer processes. *J. Petrol.* **1998**, *39*, 1641–1668. [[CrossRef](#)]
120. Zhao, J.H.; Zhou, M.F. Secular evolution of the Neoproterozoic lithospheric mantle underneath the northern margin of the Yangtze Block, South China. *Lithos* **2009**, *107*, 152–168. [[CrossRef](#)]
121. Pearce, J.A. Geochemical fingerprinting of oceanic basalts with applications to ophiolite classification and the search for Archean oceanic crust. *Lithos* **2008**, *100*, 14–48. [[CrossRef](#)]
122. Zhao, G.C. Metamorphic evolution of major tectonic units in the basement of the North China Craton: Key issues and discussion. *Acta Petrol. Sin.* **2009**, *25*, 1772–1792. (In Chinese with English Abstract)
123. Iwamori, H. Thermal effects of ridge subduction and its implications for the origin of granitic batholiths and paired metamorphic belts. *Earth Planet. Sci. Lett.* **2000**, *181*, 131–144. [[CrossRef](#)]
124. Santosh, M.; Kusky, T. Origin of paired high pressure-ultrahigh-temperature orogens: A ridge subduction and slab window model. *Terra Nova* **2010**, *22*, 35–42. [[CrossRef](#)]

125. Harley, S.L. Extending our understanding of ultrahigh temperature crustal metamorphism. *J. Mineral. Petrol. Sci.* **2004**, *99*, 140–158. [[CrossRef](#)]
126. Stüwe, K. *Geodynamics of the Lithosphere: Quantitative Description of Geological Problems*; Springer: Berlin/Heidelberg, Germany; Dordrecht, The Netherlands, 2007.
127. Hyndman, R.D.; Currie, C.A.; Mazzotti, S.P. Subduction zone back-arcs, mobile belts, and orogenic heat. *GSA Today* **2005**, *15*, 4–10. [[CrossRef](#)]
128. Brown, M. Duality of thermal regimes is the distinctive characteristic of plate tectonics since the Neoproterozoic. *Geology* **2006**, *34*, 961–964. [[CrossRef](#)]
129. Currie, C.A.; Hyndman, R.D. The thermal structure of subduction zone back arcs. *J. Geophys. Res.* **2006**, *111*, 1–22. [[CrossRef](#)]
130. Collins, W.J. Hot orogens, tectonic switching, and creation of continental crust. *Geology* **2002**, *30*, 535–538. [[CrossRef](#)]
131. Wilson, J.R.; Hansen, B.T.; Pedersen, S. Zircon U-Pb evidence for the age of the Fongen-Hyllingen complex, Trondheim region, Norway. *Geol. Fören. I Stockh. Förh.* **1983**, *105*, 68–70. [[CrossRef](#)]
132. Schärer, U.; Wilms, E.; Duchesne, J.C. The short duration and anorogenic character of anorthosite magmatism: U-Pb dating of the Rogaland complex, Norway. *Earth Planet. Sci. Lett.* **1996**, *139*, 335–350. [[CrossRef](#)]
133. Pollack, H.N. Thermal characteristics of the Archean. *Oxf. Monogr. Geol. Geophys.* **1997**, *35*, 223–232.
134. Herzberg, C.; O'hara, M.J. Plume-associated ultramafic magmas of Phanerozoic age. *J. Petrol.* **2002**, *43*, 1857–1883. [[CrossRef](#)]
135. Herzberg, C.; Condie, K.; Korenaga, J. Thermal history of the Earth and its petrological expression. *Earth Planet. Sci. Lett.* **2010**, *292*, 79–88. [[CrossRef](#)]

Disclaimer/Publisher's Note: The statements, opinions and data contained in all publications are solely those of the individual author(s) and contributor(s) and not of MDPI and/or the editor(s). MDPI and/or the editor(s) disclaim responsibility for any injury to people or property resulting from any ideas, methods, instructions or products referred to in the content.